Mon. Not. R. Astron. Soc. **000**, 1–17 (2013) Printed 11 April 2014 (MN LATEX style file v2.2)

Global simulations of magnetorotational turbulence III: influence of field configuration and mass injection

E. R. Parkin⋆
Research School of Astronomy and Astrophysics, Australian National University, Canberra, ACT 2611, Australia

arXiv:1404.2771v1 [astro-ph.HE] 10 Apr 2014

Accepted ... Received ...; in original form ...

ABSTRACT

The stresses produced by magnetorotational turbulence can provide effective angular momentum transport in accretion disks. However, questions remain about the ability of simulated disks to reproduce observationally inferred stress-to-gas-pressure ratios. In this paper we present a set of high resolution global magnetohydrodynamic disk simulations which are initialised with different field configurations: purely toroidal, vertical field lines, and nested poloidal loops. A mass source term is included which allows the total disk mass to equilibrate in simulations with long run times, and also enables the impact of rapid mass injection to be explored. Notably different levels of angular momentum transport are observed during the early-time transient disk evolution. However, given sufficient time to relax, the different models evolve to a statistically similar quasi-steady state with a stress-to-gas-pressure ratio, $\langle \alpha_{\rm P} \rangle \sim 0.032 - 0.036$. Such behaviour is anticipated based on consideration of mean magnetic field evolution subject to our adopted simulation boundary conditions.

The indication from our results is that *steady, isolated* disks may be unable to maintain a large-scale magnetic field or produce values for the stress-to-gas-pressure ratio implied by some observations. Supplementary simulations exploring the influence of trapping magnetic field, injecting vertical field, and rapidly injecting additional mass into the disk show that large stresses can be induced by these mechanisms. In the first instance, a highly magnetized disk is produced with $\langle \alpha_{\rm P} \rangle \sim 0.21$, whereas the latter cases lead to a transient burst of accretion with a peak $\langle \alpha_{\rm P} \rangle \simeq 0.1 - 0.25$. As a whole, the simulations highlight the common late-time evolution and characteristics of turbulent disks for which the magnetic field is allowed to evolve freely (i.e., without constraint/replenishment). In contrast, if the boundaries of the disk, the rate of injection of magnetic field, or the rate of mass replenishment are modified to mimic astrophysical disks, markedly different disk evolution occurs.

Key words: accretion, accretion disks - MHD - instabilities - turbulence

1 INTRODUCTION

For disk accretion to occur angular momentum must be removed from orbiting material. It has long been thought that magnetic fields could play more than just a passive role in this situation (Shakura & Sunyaev 1973; Lynden-Bell & Pringle 1974). The magnetorotational instability (MRI - Balbus & Hawley 1991, 1992, 1998) has since emerged as a robust mechanism for destabilising a differentially rotating disk, placing the importance of magnetic fields on a firm footing. Subsequent numerical work has demonstrated that the non-linear motions induced by the MRI lead to self-sustaining turbulence with the resulting stresses effectively transporting angular momentum (e.g. Hawley et al. 1995; Brandenburg et al. 1995; Stone et al. 1996).

A large body of the numerical work on magnetorotational turbulence to-date has focused on a local patch of disk with the vertical component of gravity neglected - the unstratified shearing-box. Studies examining various magnetic field configurations have produced a wide range of values for the stress-to-gas-pressure ratio, $\langle \alpha_{\rm P} \rangle \simeq 0.001 - 0.3$ (e.g. Hawley et al. 1995; Sano et al. 2004; Fromang & Papaloizou 2007; Simon et al. 2009; Guan et al. 2009, to mention but a few). Values of $\langle \alpha_{\rm P} \rangle \gtrsim 0.01$ are, however, only achieved by models initialised with a net vertical magnetic field. By construction, the unstratified shearing-box preserves an initial net vertical field. Hence, in these cases power can be effectively injected by vertical MRI modes on large spatial scales, feeding the turbulent cascade from the top down.

⋆ E-mail: ross.parkin@anu.edu.au

© 2013 RAS

Astrophysical accretion disks are, however, intrinsically global objects (by which we mean they are not periodic in the radial and/or vertical directions). Recent studies by Sorathia et al. (2010, 2012) and Beckwith et al. (2011) have demonstrated that localised patches of global disks do not preserve their magnetic field configuration in the same manner as an unstratified shearing-box. Moreover, an initial vertical field is free to evolve in global models, and it is not clear whether global disks will achieve the large stresses implied by net-vertical flux unstratified shearing-box models. What dependence of the turbulent stresses on initial field configuration should one expect for a stratified global disk? Newtonian global disk models exhibit $\langle \alpha_{\rm P} \rangle \sim 0.001 - 0.15$ (e.g. Hawley 2000; Fromang & Nelson 2006; Flock et al. 2011; Beckwith et al. 2011; Hawley et al. 2011, 2013; Parkin & Bicknell 2013a,b; Gressel et al. 2013; Parkin 2014; Suzuki & Inutsuka 2014). Larger values of $\langle \alpha_{\rm P} \rangle$ are typically associated with the saturation stress level during the initial transient phase of the simulation, with some evidence for stronger stresses when the disk initially possesses a poloidal magnetic field. There are mixed results from general relativistic global disk simulations. For instance, Beckwith et al. (2008) find markedly similar disk properties irrespective of the initial field configuration. In contrast, McKinney et al. (2012) (see also - Tchekhovskoy et al. 2011) quote $\langle \alpha_{\rm P} \rangle \sim 0.01 - 0.69$ with the lowest values for an initially toroidal field, whereas the largest values are for models where the disk initially contains a large quantity of poloidal magnetic flux.

In the present study we investigate the dependence of magnetorotational turbulence in a global disk on the initial field configuration. The simulations include a mass source term which facilitates simulations with long run times. Thus, the late-time quasi-steady disk evolution can be studied without concerns about contamination from mass exhaustion. This differs from previous global disk models, with the exception of Flock et al. (2011, 2012a,b) and Parkin (2014). A key result is the ignorance of the quasi-steady state turbulent stress, and thus efficiency of angular momentum transport, to the initial field configuration; given sufficient time the disk expels and/or digests the initial field, evolving to a statistically almost identical state. The simulations produce $\langle \alpha_{\rm P} \rangle \sim 0.032 - 0.036$ during the quasi-steady state, which falls short of observationally inferred values of $\sim 0.1 - 0.4$ (see King et al. 2007, and references therein). We perform supplementary simulations to address this quandary, finding that $\langle \alpha_{\rm P} \rangle \sim 0.2$ can be achieved by trapping field, and $\langle \alpha_{\rm P} \rangle \sim 0.1 - 0.25$ results when mass or vertical magnetic field are injected. The former case is relevant for magnetically arrested (Narayan et al. 2003) and magnetically levitating (Johansen & Levin 2008; Gaburov et al. 2012) disk models.

The remainder of this paper is organised as follows: the simulation setup and initial conditions are described in § 2. A preparatory discussion of the evolution of mean magnetic fields subject to boundary conditions is given in § 3, followed by the results of the simulations in § 4. A discussion of the implications of the results for astrophysical disks, and some potentially interesting avenues for future studies, are discussed in § 5. Finally, we close with conclusions in § 6.

2 THE MODEL

2.1 Simulation code

The global disk simulations are performed by solving the time-dependent equations of ideal magnetohydrodynamics (MHD) using the PLUTO code (Mignone et al. 2007) in a 3D spherical (r, θ, ϕ) coordinate system. The grid used for all simulations in this work has $(n_r, n_\theta, n_\phi) = (512, 256, 256)$ uniformly spaced cells, covering the spatial extent $8 < r < 34$, $\pi/2 - \theta_0 < \theta < \pi/2 + \theta_0$ (where $\theta_0 = \tan^{-1}(3H/R)$), and $0 < \phi < \pi/2$. (The θ-extent of the grid equates to $|z| \pm 3H$ for a constant aspect ratio disk.) The simulated disks all have $H/R = 0.1$, where H is the disk scale height. In terms of cells per scale height, the adopted grid has $(n_r/H, n_\theta/H, n_\phi/H) \simeq (16{-}67, 44, 16)$ which is comfortably within the regime of convergence with resolution detailed by Parkin & Bicknell (2013b). The simulations are performed in scaled units: $\rho_{\rm scale} = 1.67 \times 10^{-7}$ gm s^{-1}, $v_{\rm scale} = c$ (where c is the speed of light), $T_{\rm scale} = \mu m c^2 / k_{\rm B} = 6.5 \times 10^{12}$ K, $l_{\rm scale} = 1.48 \times 10^{13}$ cm, and the value of $l_{\rm scale}$ corresponds to the gravitational radius of a 10^8 M$_\odot$ black hole.

The adopted numerical setup closely follows that of Parkin (2014) - a detailed description can be found there-in. In brief, PLUTO code was configured to use the five-wave HLLD Riemann solver of Miyoshi & Kusano (2005), piecewise parabolic reconstruction (PPM - Colella & Woodward 1984), limiting during reconstruction on characteristic variables (e.g. Rider et al. 2007), second-order Runge-Kutta time-stepping, the upwind Constrained Transport scheme (Gardiner & Stone 2005), and the FARGO-MHD module (Mignone et al. 2012). A mass source term is included which relaxes the gas density in the region $31 \leqslant r \leqslant 34$, $|z| < 2H$ towards the initial density distribution over a timescale of an orbital period, where H is the thermal disk scale-height. This latter addition allows the total mass and energies in the disk to stabilise, permitting long run-time global disk simulations which avoid the restriction of exhausting the mass supply (Flock et al. 2011; Parkin 2014).

The adopted boundary conditions are identical to those used in Parkin (2014), with the exception that for model VERT-TRAP the radial velocity at the inner radial boundary is set to $v_r = -(3/2)\alpha_{\rm P} c_{\rm s}^2 / \Omega r$, where $c_{\rm s}$ is the sound speed, Ω is the angular velocity, and $\alpha_{\rm P}$ is the Shakura & Sunyaev (1973) α-parameter (see Eq 13). This equates to fixing the radial velocity to a viscous outflow rate and has been used previously by Fromang & Nelson (2006) and Suzuki & Inutsuka (2014) to reduce the rate at which mass exits the grid. In the present study this boundary condition is utilised to deliberately trap magnetic field, by adopting $\alpha_{\rm P} = 0.001$ in the equation for v_r (which is lower than the $\langle \alpha_{\rm P} \rangle = 0.032 - 0.036$ produced by the turbulent disk).

2.2 Outline of simulations performed

Simulations are performed to examine the following topics (details are summarised in Table 1):

- *Initial field configuration*: The primary aim of this study is to investigate the influence of different initial magnetic field topologies on the subsequent non-linear evolution of turbulence in a disk. To this end we examine three different initial field topologies: i) a purely toroidal magnetic field

Table 1. Summary of simulations. β_0 is the plasma-β of the initial magnetic field.

Model	Initial field	β_0	Comment
TOR-β20	Toroidal	20	Fiducial model
TOR-β1	Toroidal	1	Low β_0
VERT	Vertical	2000	Vertical field
LOOP	Poloidal loops	300	Zero-net flux field
VERT-TRAP	Vertical	2000	Restricted radial outflow
VERT-B+	Vertical	2000	Testing B_θ injection
TOR-M+	Toroidal	20	Testing mass injection

(models TOR-β20 and TOR-β1), ii) purely vertical magnetic field (model VERT), and, iii) concentric nested loops of poloidal magnetic field (model LOOP).

• *Strongly magnetized disk*: Model TOR-β1 examines the affect on both early- and late-time disk evolution associated with a strong initial magnetic.

• *Trapping of magnetic field*: Model VERT-TRAP is a repeat of model VERT with an intentionally restrictive outflow boundary condition used at the inner radial boundary, allowing the influence of field trapping on the disk evolution to be examined.

• *Injection of vertical magnetic field*: Model VERT-B+ explores the disk evolution when a vertical magnetic field is steadily added to the simulation domain.

• *Transient accretion induced by rapid mass injection*: A supplementary simulation (model TOR-M+) has been performed for which the mass source term (described in § 2.1) is modified to inject mass rapidly over a short duration of time, resulting in a transient burst in accretion activity in the disk. Further details of model TOR-M+ are given in § 4.4.

2.3 Initial conditions

For models TOR-β20 and TOR-β1 we use the exact equilibrium torus of Parkin & Bicknell (2013a) with the ratio of gas-to-magnetic pressure, $\beta = 2p/|B|^2 \equiv 2p/B_\phi^2$ initially set to 20 and 1, respectively. The magnetic field is net-flux and purely toroidal, with a constant β throughout the disk. The density distribution of this disk in cylindrical (R, z) coordinates is given by,

$$\rho(R,z) = \rho(R,0)\exp\left(\frac{-(\Phi(R,z)-\Phi(R,0))}{T(R)}\frac{\beta}{1+\beta}\right), \quad (1)$$

where $p = \rho T$, and $T = T(R)$ is the (isothermal in height) temperature. For the radial profiles $\rho(R,0)$ and $T(R)$ in Eq (1) we use simple functions inspired by the Shakura & Sunyaev (1973) disk model:

$$\rho(R,0) = \rho_0 f(R, R_0, R_{\rm out})\left(\frac{R}{R_0}\right)^{\epsilon}, \quad (2)$$

$$T(R) = T_0\left(\frac{R}{R_0}\right)^{\eta}, \quad (3)$$

where ρ_0 sets the density scale, R_0 and $R_{\rm out}$ are the radius of the inner and outer disk edge, respectively, $f(R, R_0, R_{\rm out})$ is a tapering function that truncates the density profile at a specified inner and outer radius (Parkin & Bicknell 2013a), and ϵ and η set the slope of the density and temperature profiles, respectively. Values are set to $R_0 = 7$, $R_{\rm out} = 50$, $\rho_0 = 10$, $\epsilon = -33/20$, $\eta = -9/10$, and $T_0 = 1.5 \times 10^{-3}$, producing a disk with $H/R = 0.1$. The rotational velocity of the disk is,

$$v_\phi^2(R,z) = v_\phi^2(R,0) + (\Phi(R,z) - \Phi(R,0))\frac{R}{T}\frac{dT}{dR}, \quad (4)$$

where,

$$v_\phi^2(R,0) = R\frac{\partial\Phi(R,0)}{\partial R} + \frac{2T}{\beta} + \left(\frac{1+\beta}{\beta}\right)\left(\frac{RT}{\rho(R,0)}\frac{\partial\rho(R,0)}{\partial R} + R\frac{dT}{dR}\right). \quad (5)$$

The (purely toroidal) magnetic field is initialised using the θ-component of the vector potential,

$$A_\theta = \frac{1}{r}\int_{r_0}^{r} rB_\phi {\rm d}r, \quad (6)$$

where $r_0 = 7$ and $A_\theta(r \leqslant r_0) = 0$. The reader is referred to Parkin & Bicknell (2013a) and Parkin (2014) for further details of the initial conditions for model TOR-β20.

For the poloidal field models (VERT, LOOP, VERT-TRAP, and VERT-B+) the initial conditions consist of an isothermal-in-height disk ($T = T(R)$) which is in hydrodynamic equilibrium. The equations for the density and rotational velocity in this case are found from the $\beta \to \infty$ limit of Eqs (1) and (5). The magnetic field is initialised in the poloidal field models using the ϕ-component of the vector potential. For models VERT, VERT-TRAP, and VERT-B+ we use,

$$A_\phi \propto \frac{1}{2R}(R^2 - R_0^2), \quad (7)$$

with $R_0 = 7$. The value of A_ϕ in Eq (7) is scaled to give a disk averaged initial field strength with $\beta \simeq 2000$. For model LOOP we initialise the magnetic field via:

$$\begin{array}{ll} A_\phi \propto & (\rho/\rho_0)\sin(k_{\rm loop}(R-R_1)); \quad R_1 < R < R_2, \\ A_\phi = & 0; \qquad\qquad\qquad\qquad\quad \text{otherwise}, \end{array} \quad (8)$$

where ρ_0 is the disk density at $(R = R_0, z = 0)$, $k_{\rm loop} = \pi n_{\rm loop}/(R_2 - R_1)$, $n_{\rm loop} = 10$ is the number of loops, $R_0 = 7$, $R_1 = 10$, and $R_2 = 30$. This produces a zero-net poloidal flux field consisting of ten concentric loops between $10 < R < 30$. Equation (8) is scaled to give a disk-averaged $\beta \simeq 300$.

In all models, we initiate the development of turbulence by adding random poloidal velocity fluctuations of amplitude 0.01 $c_{\rm s}$ to the initial equilibrium.

3 MEAN FIELD EVOLUTION

Three-dimensional power spectra computed from turbulent global disk models show that the majority of energy is contained in scales on the order of $\sim 2H$ (Parkin & Bicknell 2013b; Parkin 2014). In such a case volume-averaged mean fields are a proxy for large-scale fields, which follows from the integral transform relation between length scales and wavenumber space (i.e. Parseval's theorem). Moreover, the injection of energy into the turbulent cascade on large scales requires large-scale field components, so that tracking the evolution of mean magnetic fields provides information about the ability of the field configuration to inject energy

at the upper end of the cascade. The simulation boundary conditions influence the evolution of mean magnetic fields, and in the following we examine the consequences of our adopted setup. (For further discussion of these points, and the associated impact on the convergence properties of different numerical setups, see Parkin & Bicknell 2013b and references therein.)

Let us consider the volume averaged induction equation for the radial, vertical (θ-direction), and azimuthal magnetic fields, respectively,

$$\frac{\partial}{\partial t}\langle B_r\rangle = -\frac{1}{V}\int_{\theta_2}\mathcal{E}_\phi\,\mathrm{d}s_\theta + \frac{1}{V}\int_{\theta_1}\mathcal{E}_\phi\,\mathrm{d}s_\theta, \tag{9}$$

$$\frac{\partial}{\partial t}\left\langle\frac{B_\theta}{r}\right\rangle = \frac{1}{V}\int_{r_2}\frac{\mathcal{E}_\phi}{r}\mathrm{d}s_r - \frac{1}{V}\int_{r_1}\frac{\mathcal{E}_\phi}{r}\mathrm{d}s_r \tag{10}$$

and,

$$\frac{\partial}{\partial t}\left\langle\frac{B_\phi}{r\sin\theta}\right\rangle = -\frac{1}{V}\int_{r_2}\frac{\mathcal{E}_\theta}{r\sin\theta}\mathrm{d}s_r + \frac{1}{V}\int_{r_1}\frac{\mathcal{E}_\theta}{r\sin\theta}\mathrm{d}s_r - \frac{1}{V}\int_{\theta_2}\frac{\mathcal{E}_r}{r\sin\theta}\mathrm{d}s_\theta + \frac{1}{V}\int_{\theta_1}\frac{\mathcal{E}_r}{r\sin\theta}\mathrm{d}s_\theta \tag{11}$$

where $V = \iiint dV$ is the volume bound by the surfaces, $\mathrm{d}s_r = r^2\sin\theta\,\mathrm{d}\theta\,\mathrm{d}\phi$, $\mathrm{d}s_\theta = r\sin\theta\,\mathrm{d}r\,\mathrm{d}\phi$. The θ- and ϕ-components of the electric field are given by $\mathcal{E}_\theta = v_r B_\phi - v_\phi B_r$ and $\mathcal{E}_\phi = v_\theta B_r - v_r B_\theta$, respectively. Angle-brackets denote a volume-average, e.g.,

$$\langle q\rangle = \frac{\iiint q\,r^2\sin\theta\mathrm{d}r\,\mathrm{d}\theta\,\mathrm{d}\phi}{\iiint r^2\sin\theta\,\mathrm{d}r\,\mathrm{d}\theta\,d\phi}. \tag{12}$$

From Eq (10) one sees that the vertical field can evolve when the radial boundaries are open, which is the case for the global disk simulations in this work. In contrast, the initial mean vertical magnetic field is preserved in shearing-box studies employing a radially periodic boundary condition - see Hawley et al. (1995) for further details. Shearing-box models do not, therefore, allow one to investigate questions of if/how a vertical magnetic field is preserved because the vertical field evolution is constrained by the simulation setup. Vertical field can naturally disperse through radial boundaries in the global models considered in this work, and the tendency in the simulations is for the initial field configuration to advect off the grid in the accretion flow.

Considering Eqs (10) and (11) in more detail, the rate of dispersal of the initial field configuration can be limited by, for example, restricting the radial outflow velocity at the boundaries because v_r features in both $\mathcal{E}_\theta$ and $\mathcal{E}_\phi$. This effect is explored with model VERT-TRAP in § 4.2, where it is found that trapping vertical and azimuthal magnetic field leads to drastically different disk evolution. Alternatively, the mean vertical field strength may be altered by adding magnetic field to the domain, which is explored using model VERT-B+ in § 4.3.

4 RESULTS

4.1 Influence of initial field topology in isolated disks

In this section we begin our investigation by considering models with different initial field configurations and their respective evolution when allowed to evolve freely. In this regard models TOR-β1, TOR-β20, VERT, and LOOP represent isolated accretion disks with no external influence and a limited source of magnetic field. In § 4.2, 4.3, and 4.4 we consider models with modified boundary conditions, magnetic field injection, and mass injection. These additional models are geared towards exploring possible external influences on the evolution of the disk turbulence.

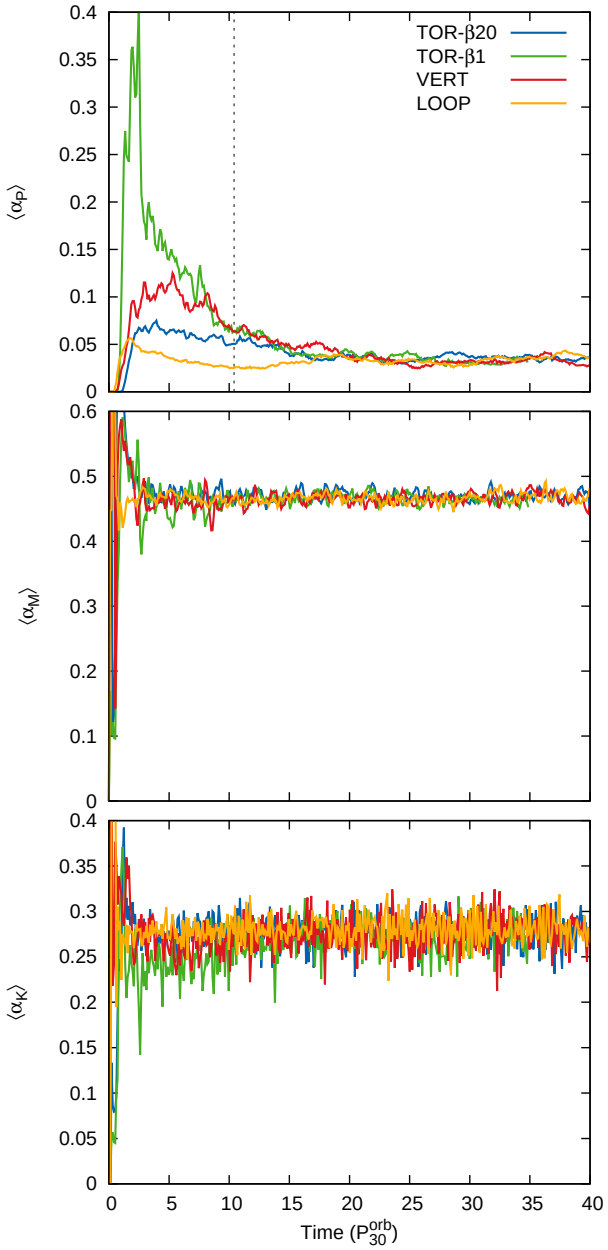

Figure 1. The time evolution of $\langle\alpha_\mathrm{P}\rangle$ (upper), $\langle\alpha_\mathrm{M}\rangle$ (middle), and $\langle\alpha_\mathrm{K}\rangle$ (lower) computed for the disk body ($15 < r < 25$, $|z| < 2H$). Time is in units of the orbital period at a radius of $r = 30$, P_{30}^{orb}. (For comparison, $P_{30}^{\mathrm{orb}} = 9\,P_{8}^{\mathrm{orb}}$, therefore roughly 360 inner disk orbits are covered.) Corresponding time averaged results are given in Table 2. The vertical dashed line in the upper panel indicates the simulation run time for the models presented by Hawley et al. (2013).

Table 2. List of time averaged quantities computed for the simulations. For all models values are spatially averaged within the disk body ($15 < r < 25$, $|z| < 2H$) and time averaged over the interval $20 \leqslant t \leqslant 40\ P_{30}^{\rm orb}$, except for model TOR-$\beta$1 where the time average is between $20 \leqslant t \leqslant 35\ P_{30}^{\rm orb}$.

Parameter	TOR-β20	TOR-β1	VERT	LOOP	VERT-TRAP
M_0	5477	6759	5376	5376	5376
$M_{\rm QSS}$	1814	1779	1870	2118	424
$\langle\alpha_{\rm P}\rangle$	0.036	0.034	0.032	0.034	0.21
$\langle\alpha_{\rm M}\rangle$	0.469	0.466	0.467	0.467	0.466
$\langle\alpha_{\rm K}\rangle$	0.279	0.273	0.278	0.280	0.176
$-\langle B_r' B_\phi'\rangle/\langle\rho v_r' v_\phi'\rangle$	2.69	2.55	2.55	2.63	5.71
$\dot{M}_{\rm rad}$ $(P_{30}^{\rm orb-1})$	160	156	159	154	260
$\dot{M}_{\rm vert}$ $(P_{30}^{\rm orb-1})$	23	29	18	22	154
$N_{\rm r}$	0.76	0.76	0.74	0.75	0.95
N_θ	0.65	0.64	0.62	0.64	0.93
N_ϕ	0.81	0.80	0.79	0.80	0.96
$\langle\beta_{\rm r}\rangle$	118	129	139	131	10
$\langle\beta_\theta\rangle$	316	340	369	347	18
$\langle\beta_\phi\rangle$	20	21	22	21	1.8
$\langle\beta_{\rm tot}\rangle$	16	17	18	17	1.4
$\langle B_r\rangle$ $(\times 10^{-3})$	0.002 ± 0.004	-0.001±0.005	0.001 ± 0.003	0.003 ± 0.004	-0.098 ± 0.015
$\langle B_\theta\rangle$ $(\times 10^{-3})$	0.033 ± 0.001	0.0002 ± 0.0019	-0.012 ± 0.001	0.006 ± 0.002	-0.13 ± 0.01
$\langle B_\phi\rangle$ $(\times 10^{-3})$	0.090 ± 0.071	0.14±0.09	0.036 ± 0.063	-0.25 ± 0.06	2.86 ± 0.52

4.1.1 Turbulent stresses

The simulations performed in this work aim to explore the differences in the ensuing turbulent state arising from different initial field topology. The models TOR-β20, TOR-β1, VERT, and LOOP start from an almost identical disk (in terms of density, temperature, and rotation velocity distributions) but differ in the initial strength and topology of the magnetic field[1]. As the simulations evolve, the perturbations introduced into the initial conditions excite the MRI. Because of the different field topologies and field strengths in the models the respective initial MRI growth rates differ. Consequently, the resultant stresses arising during the initial transient disk evolution are not the same between the simulations. An indication of the differences in the turbulent stresses during the initial transient phase can be gained from the Shakura & Sunyaev (1973) α-parameter, which we define as the $r-\phi$ component of the combined Reynolds and Maxwell stress normalised by the gas pressure,

$$\langle\alpha_P\rangle = \frac{\langle\rho v_r' v_\phi' - B_r' B_\phi'\rangle}{\langle p\rangle}, \tag{13}$$

where primes denote a fluctuating (turbulent) deviation from an azimuthal mean, such that,

$$v_{\rm i} = v_i' + \bar{v}_i, \quad \text{where,} \quad \bar{v}_i = [\rho v_i]/[\rho], \tag{14}$$

and,

$$B_i = B_{\rm i}' + \bar{B}_i, \quad \text{where,} \quad \bar{B}_i = [B_i], \tag{15}$$

where over-bars indicate a mean and square brackets indicate an azimuthal average,

$$[q] = \frac{\int qr\sin\theta d\phi}{\int r\sin\theta d\phi}. \tag{16}$$

[1] Model TOR-β20 was previously presented by Parkin (2014) in the context of turbulent energetics and further detailed analysis of this simulation may be found therein.

Note that we use density-weighted averages to compute the mean velocities, consistent with the analytical approach of Kuncic & Bicknell (2004) - see also Parkin (2014). The volume averages in Eq (13), and in all other instances in this work, are taken over the region $15 < r < 25$, $|z| < 2H$, and the entire azimuthal extent of the domain, $0 < \phi < \pi/2$.

Fig. 1 shows that over the first 10 $P_{30}^{\rm orb}$ of the simulations (where $P_{30}^{\rm orb}$ corresponds to the orbital period at a radius, $r = 30$) model TOR-β1 has the highest $\langle\alpha_{\rm P}\rangle$, followed by VERT, TOR-$\beta$20, and then LOOP. The prominent spike in $\langle\alpha_{\rm P}\rangle$ for model TOR-β1 is associated with the rapid development of large-scale, non-axisymmetric MRI modes, powered by the strong toroidal field. In contrast, the relatively large transient stresses for model VERT result from vertical MRI mode growth, with an additional contribution from parasitic instabilities feeding on channel flows (Goodman & Xu 1994).

The dependence of the turbulent stress on initial field topology was recently examined by Hawley et al. (2013) using high resolution global disk simulations. Given the similarity in their goals to the present study, a comparison is warranted. However, we note that the simulations presented by Hawley et al. (2013) were only run until a time of $t \simeq 10.4\ P_{30}^{\rm orb}$ (indicated by the vertical dashed line in the upper panel of Fig. 1) which, as noted by the authors, was the result of the limitations of a finite disk mass. Within this time interval - which covers the transient evolution phase close to the beginning of the simulation - our results agree with Hawley et al. (2013) in that there is a clear dependence of the peak saturation stress level on the initial field topology. However, there are some differences in the details. For instance, Hawley et al. (2013) found that a higher saturation stress was achieved by a simulation with two poloidal loops compared to one with a toroidal field. In contrast, we find the highest saturation stress for a toroidal field model with $\beta = 1$ initially (TOR-β1), with the lowest stress level for a model with ten concentric poloidal loops (model LOOP).

Focusing on the latter half of the simulations in Fig. 1, one sees that the turbulence evolves to be markedly similar in the different models. Indeed, time-averaged values are in the range $\langle\alpha_{\rm P}\rangle = 0.032 - 0.036$ (noted in Table 2) which is consistent with the converged quasi-steady state found by Parkin & Bicknell (2013b) for a toroidal field disk similar to TOR-β20. Importantly, this demonstrates that given sufficient time an isolated turbulent accretion disk evolves to a state that is identical, irrespective of the initial magnetic field configuration. Thus, we concur with Hawley et al. (2013) that the turbulent stress *during the initial transient phase* depends on the initial field configuration, whereas our results show that the late-time quasi-steady stresses (i.e. at $t > 20\,P_{30}^{\rm orb}$) do not. Implications of this finding for explaining observations of astrophysical disks are discussed in § 5.

Further similarities between the late-time evolution of the models are found in the parameters $\langle\alpha_{\rm M}\rangle$ and $\langle\alpha_{\rm K}\rangle$, which are defined to be the $r-\phi$ component of the Maxwell stress normalised by the magnetic pressure,

$$\langle\alpha_{\rm M}\rangle = \frac{\langle -2B_r'B_\phi'\rangle}{\langle |B'|^2\rangle}, \tag{17}$$

and the $r-\phi$ component of the Reynolds stress normalised by the turbulent kinetic energy,

$$\langle\alpha_{\rm K}\rangle = \frac{\langle \rho v_r' v_\phi'\rangle}{\langle u_{\rm K'}\rangle}, \tag{18}$$

where $\langle u_{\rm K'}\rangle = \frac{1}{2}\rho|v'|^2$. The importance of the parameter $\langle\alpha_{\rm K}\rangle$ resides in turbulent kinetic energy generation and the significant role of the correlation between Reynolds stresses with mean flow shear as an energy injection term (Balbus & Hawley 1998; Kuncic & Bicknell 2004; Parkin 2014). During the latter half of the simulation $\langle\alpha_{\rm M}\rangle$ and $\langle\alpha_{\rm K}\rangle$ reach quasi-steady values of ~ 0.47 and ~ 0.28, respectively, with little difference between models TOR-β1, TOR-β20, VERT, and LOOP (Table 2). The values of $\langle\alpha_{\rm K}\rangle$ from the models are consistent with, but slightly higher than, the value of 0.25 reported for stratified shearing-box models by Brandenburg et al. (1995). We note that $\langle\alpha_{\rm M}\rangle$ reaches a steady value faster than $\langle\alpha_{\rm P}\rangle$, allowing safe comparisons to be made against previous shorter run time global models. As such, we find good agreement for time averaged values of $\langle\alpha_{\rm M}\rangle$ with the studies by Hawley et al. (2011, 2013), Beckwith et al. (2011), and Parkin & Bicknell (2013a,b). The ratio of Maxwell-to-Reynolds stress, $-\langle B_r'B_\phi'\rangle/\langle\rho v_r'v_\phi'\rangle = 2.55-2.69$ is also consistent with previous global disk studies (Fromang & Nelson 2006; Beckwith et al. 2011; Parkin 2014).

4.1.2 Disk structure

Following the development of the MRI in the simulations, the disk structure in models TOR-β1, TOR-β20, VERT, and LOOP evolves towards a quasi-steady state. The time evolution of vertical profiles of the gas density, toroidal magnetic field, plasma-β, and turbulent gas velocity are shown for model VERT in Fig. 2. During the initial transient phase at the start of the simulation the rapid growth of accretion stresses drives mass out of the disk. At later times the density distribution in the disk reaches a close equilibrium between mass inflow/outflow. The heightened level of turbulent activity during the transient phase is evident from the turbulent gas velocity, which rises at the start of the run and

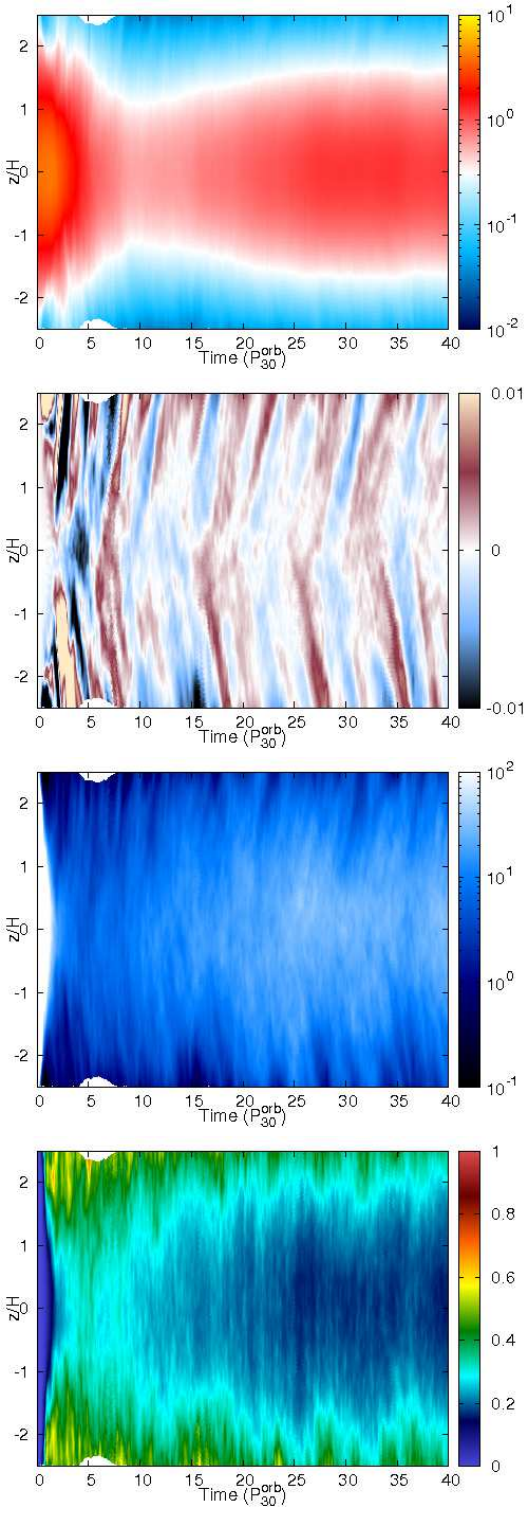

Figure 2. Time evolution of vertical profiles of various quantities in model VERT. Shown are: density (top), B_ϕ (upper middle), plasma-β (lower middle), and the magnitude of the turbulent velocity normalised to the sound speed. To construct the profiles the simulation data was azimuthally averaged over the entire ϕ-extent of the domain and radially between $15 < r < 25$.

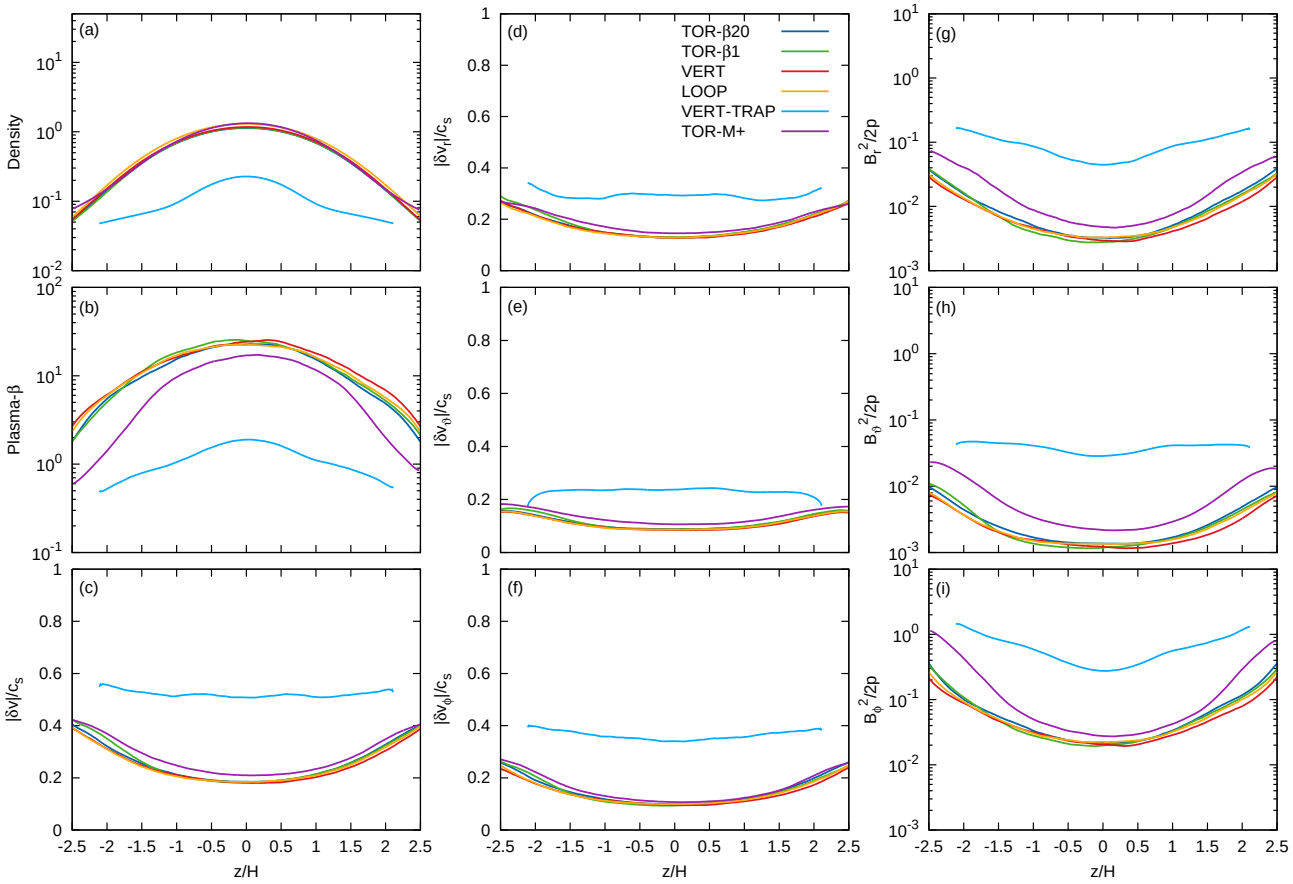

Figure 3. Vertical profiles of various quantities in the simulations. To construct the profiles the simulation data was azimuthally averaged over the entire ϕ-extent of the domain, radially between $15 < r < 25$, and then time averaged over the time interval $20 < t < 40\ P_{30}^{\rm orb}$ (except for model TOR-M+ where the interval $25 < t < 40\ P_{30}^{\rm orb}$ was used). Shown are: (a) density, (b) plasma-β ($= 2p/B^2$), (c) turbulent gas velocity normalised to sound speed, (d)-(f) r, θ, and ϕ turbulent velocity components normalised to the sound speed, and (g)-(i) r, θ, and ϕ magnetic pressure normalised to gas pressure.

then falls at later times. There is a coincident rise and fall in magnetic field strength, illustrated by the plasma-β parameter. Quasi-periodic oscillations indicative of dynamo cycles are apparent in the toroidal magnetic field (upper middle panel in Fig. 2). The oscillation period of 4 $P_{30}^{\rm orb}$ is in good agreement with that observed in previous shearing-box (e.g. Davis et al. 2010; Gressel 2010; Shi et al. 2010; Simon et al. 2012) and global models (Beckwith et al. 2011; Flock et al. 2012a; Parkin 2014; Suzuki & Inutsuka 2014). Interestingly, much shorter period fluctuations can be seen in the plasma-β and turbulent velocity, which may be associated with the intermittency of the turbulence, or a secondary cycle.

Examining the vertical structure of the simulated disks (time-averaged over the latter half of the run) one sees markedly similar profiles for model TOR-β1, TOR-β20, VERT, and LOOP. The gas density (Fig. 3(a)) follows a roughly Gaussian shape, consistent with previous global disk studies (e.g. Flock et al. 2011; Suzuki & Inutsuka 2014). The magnetic field strength is sub-thermal close to the mid plane, illustrated by $\beta \gg 1$ in Fig 3(b) at $z \simeq 0$, and rises ($\beta \to 1$) with increasing height in agreement with Fromang & Nelson (2006), Flock et al. (2011), Beckwith et al. (2011), and Parkin (2014). Similarly, the turbulent gas velocities are lowest close to the mid plane, being subsonic at all heights, and increasing as one tends towards the upper/lower grid boundary. Inspecting the separate components of the turbulent gas velocity, shown in Fig 3(d)-(f), the radial and azimuthal fluctuations are larger than those in the vertical direction. Similar behaviour for turbulent gas velocities was observed by Fromang & Nelson (2006); Flock et al. (2011); Beckwith et al. (2011), and Parkin (2014), who found $|\delta v|/c_{\rm s} \simeq 0.1$ at the mid plane for the different velocity components.

4.1.3 Mass-loss

The establishment of turbulence and associated angular momentum transport in the simulations leads to evolution of the total disk mass, as illustrated by Fig. 4. All of the models show a decrease in the total disk mass during the transient evolution phase, followed by a flattening as the turbulent activity subsides and a balance is reached between rates of mass leaving and entering the disk via accretion and mass injection, respectively. The total disk mass during the quasi-steady state, $M_{\rm QSS}$, is noted in Table 2. Reasonable agreement is seen in $M_{\rm QSS}$ between models TOR-β1, TOR-β20, VERT, and LOOP, despite TOR-β1 having a slightly higher

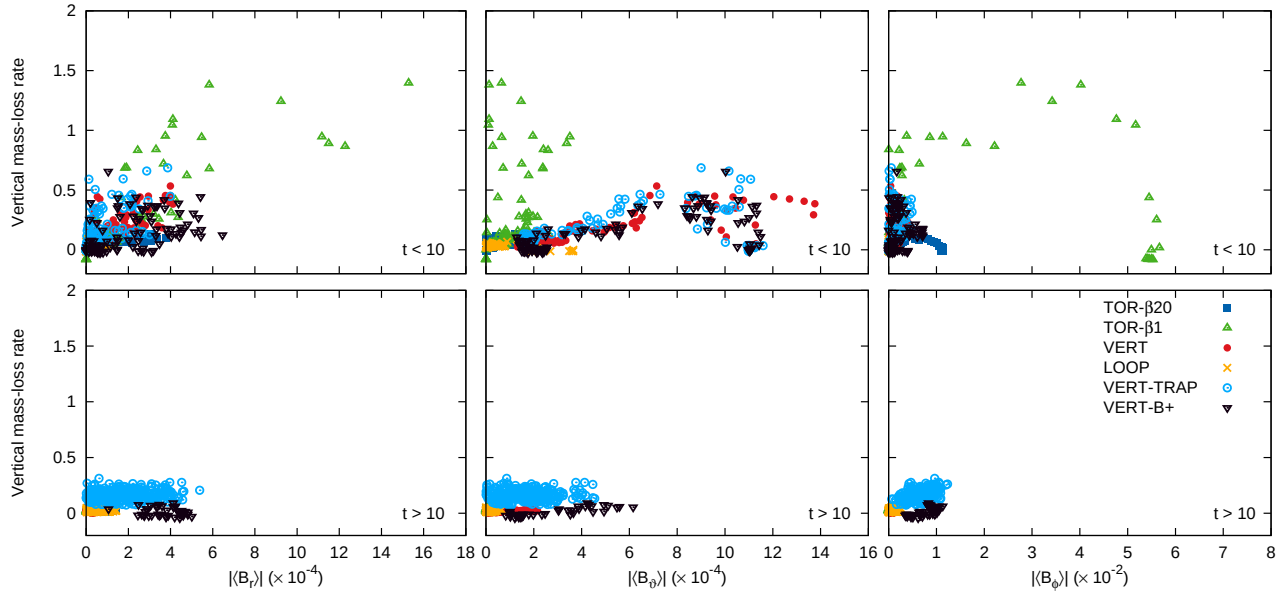

Figure 5. Correlation between the vertical mass-loss rate, $\dot{M}_{\rm vert}$, and the magnitude of the volume averaged magnetic field. The columns (from left to right) show the correlation with: $|\langle B_r \rangle|$, $|\langle B_\theta \rangle|$, and $|\langle B_\phi \rangle|$. The upper and lower rows show data points sampled every $0.1\,P_{30}^{\rm orb}$ from the time intervals $t < 10\,P_{30}^{\rm orb}$ and $t > 10\,P_{30}^{\rm orb}$, respectively.

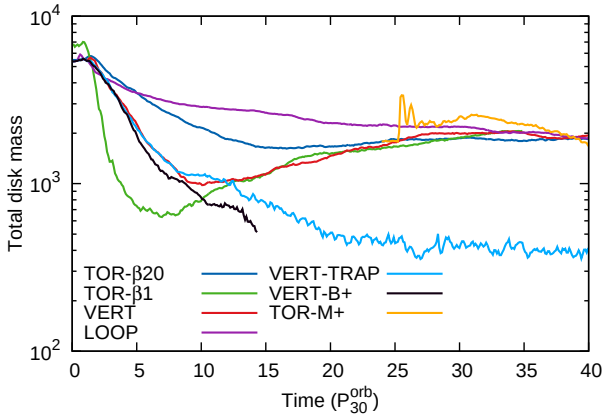

Figure 4. The evolution of the total disk mass. Corresponding time-averaged values can be found in Table 2.

initial disk mass of $M_0 = 6759$ (compared to $5376 - 5477$ for the other models). On average, the total disk mass during the quasi-steady state is 33% of the initial disk mass.

Surface integrated mass fluxes have been computed to assess the rates at which mass is leaving the disk in the radial, $\dot{M}_{\rm rad}$, and vertical, $\dot{M}_{\rm vert}$, directions. It is clear from Table 2 that the radial mass flux dominates over the vertical mass flux for models TOR-β1, TOR-β20, VERT, and LOOP.

Models of stratified disks with a net vertical magnetic field, in both the shearing-box[2] and global setting, suggest a strong correspondence between the vertical magnetic field strength and the rate of vertical mass-loss (Suzuki & Inutsuka 2009, 2014; Bai & Stone 2013). To examine whether a similar trend is observed in the global disk models presented in this work, in Fig. 5 we plot data-points for $\dot{M}_{\rm vert}$ and $|\langle B \rangle|$. For all models except TOR-β1 there is a suggestion that larger $\dot{M}_{\rm vert}$ values are coincident with a stronger vertical magnetic field strength ($|\langle B_\theta \rangle|$). This is most clearly seen at early times in the simulations (top row of Fig. 5). However, a contrasting trend is seen for model TOR-β1, where the largest vertical mass-loss rates arise during the transient phase of the simulation when $|\langle B_\theta \rangle|$ is relatively small. Interestingly, the large $\dot{M}_{\rm vert}$ at early times ($t < 10\ P_{30}^{\rm orb}$) in TOR-β1 correlates well with radial magnetic field ($|\langle B_r \rangle|$), with a weaker correlation with the azimuthal magnetic field ($|\langle B_\phi \rangle|$). The data points for TOR-β1 in the top row of Fig. 5 are consistent with vertical mass-loss resulting from stresses and magnetic pressure gradients associated with the disruption of the strong toroidal field during the early-time transient phase.

Before closing this section it is pertinent to recall an important finding from the recent study by Fromang et al. (2013), namely that the vertical mass-loss rate depends on the vertical extent of the simulation domain. This behaviour is linked to the position of the critical points of the wind launching, and whether the adopted vertical grid extent captures all of the relevant critical points. Due to the large computational expense of performing global disk simulations at the resolution of the models presented in this work, we must defer a comprehensive study of similar models with considerably larger vertical extent to a future study. As such, we urge that the differences in vertical mass-loss rate between

[2] It is noteworthy that the mean radial and azimuthal magnetic field can evolve in a stratified shearing-box whereas the mean vertical field cannot (see § 3 and Parkin & Bicknell 2013b, for further discussion). Therefore, it is the magnitude of the vertical component of the initial magnetic field, and not the field topology that is critical for shearing-box models.

the models in this work should be taken as illustrative (because the flow velocities are subsonic as the gas exits the vertical grid boundary). Further work will be needed to establish the exact quantitative details of magnetic flux transport in thin accretion disks possessing a large-scale vertical field, and whether inward or outward radial flux transport occurs (see, e.g., Lubow et al. 1994; Beckwith et al. 2009; Guilet & Ogilvie 2012; McKinney et al. 2012).

4.1.4 Resolution of the MRI

To demonstrate that the simulations are sufficiently well resolved, and that their common late-time evolution is not an artefact of under-resolved MRI modes, we calculate a resolvability factor, $N_{\rm i}$, which is defined to be the fraction of cells in the disk body that resolve the wavelength of the fastest growing MRI mode, $\lambda_{\rm MRI-i}$, with at least 8 cells[3]. Defining,

$$\lambda_{\rm MRI-i} = \frac{2\pi |v_{\rm Ai}| r \sin\theta}{v_\phi}, \qquad (19)$$

where $i = r, \theta, \phi$, and $v_{\rm Ai} = B_{\rm i}/\sqrt{\rho}$ is the Alfvén speed. Time-averaged values for the resolvability factors (computed for the quasi-steady turbulent state) are noted in Table 2. The values are similar between the models, consistent with their broad similarity during the latter half of the runs. Moreover, the values are indicative of well-resolved MRI-driven turbulence (Sorathia et al. 2012; Parkin & Bicknell 2013b).

4.1.5 Magnetic field evolution

The behaviour of the magnetic energies in the different models is in keeping with their respective initial field topologies (Fig. 6). For instance, defining the plasma-β as $\beta_i = |B_i|^2/2p$, where $i = r, \theta, \phi$ or "tot" (i.e. all components), models TOR-β1 and TOR-β20 are clearly dominated by toroidal magnetic field during the first few orbits, whereas model VERT (which started with a purely vertical field) has a smaller $\langle\beta_\theta\rangle$ initially. In fact, after a few orbits, the conversion of poloidal magnetic field into toroidal field by the disk rotation results in $\langle\beta_\phi\rangle$ clearly dominating $\langle\beta_{\rm tot}\rangle$ in all of the models. Consistent with the diagnostics discussed in the previous sections, during the quasi-steady state ($20 < t < 40\,P_{30}^{\rm orb}$), the evolution of β in models TOR-β1, TOR-β20, VERT, and LOOP closely matches one another. Time-averaged values are also in good agreement (Table 2). Curiously, the vertical magnetic field strength is weakest for model VERT, despite it possessing the strongest vertical field in the initial conditions. However, the indication from the plot of $\langle\alpha_{\rm P}\rangle$ in Fig. 1 is that the transient phase lasts the longest for this model. Hence, a prolonged phase with a higher accretion rate will drain the poloidal magnetic fields from the disk. The evolution of the mean magnetic fields, discussed below, supports this explanation.

[3] This equates to measuring the fraction of cells which have a "quality factor" (Noble et al. 2010; Hawley et al. 2011) which is 8 or better throughout the disk - see also Sorathia et al. (2012) and Parkin & Bicknell (2013b).

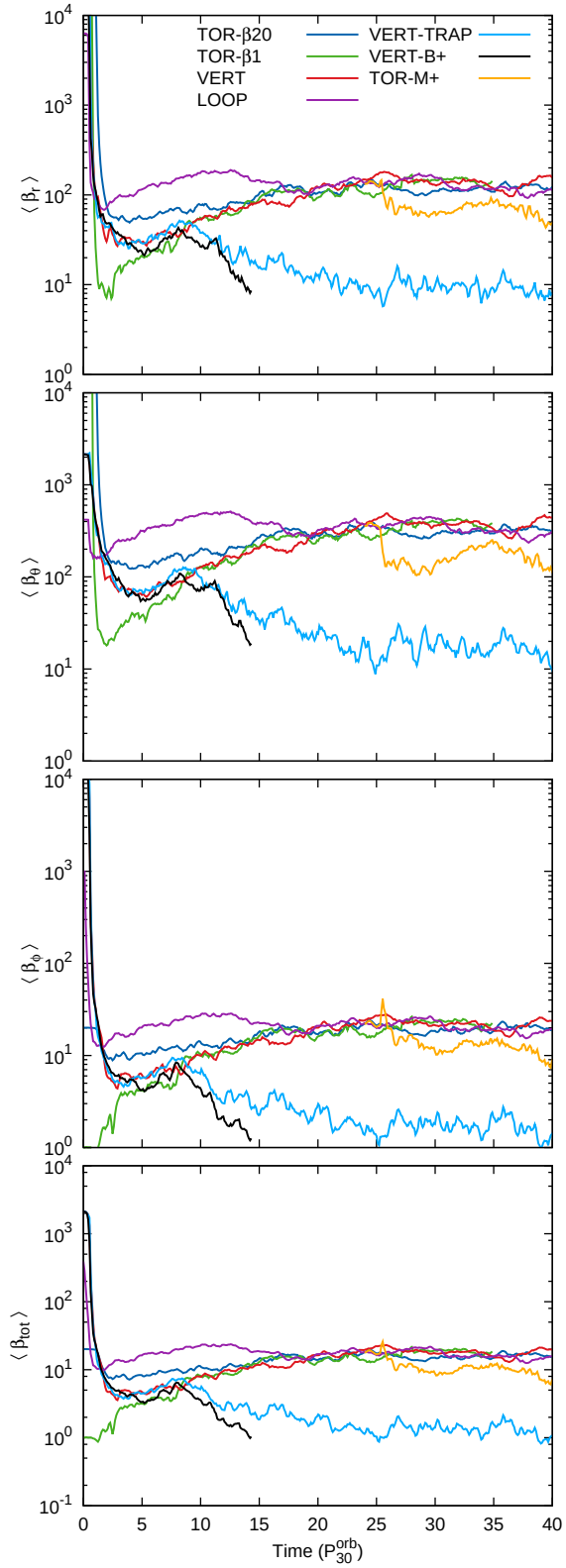

Figure 6. The volume-averaged (over the region $15 < r < 25, |z| < 2H$) plasma-β for models TOR-β20, TOR-β1, VERT, LOOP, VERT-TRAP, and TOR-M+. Respective plasma-β values for different magnetic field components are shown (from top to bottom): $\langle\beta_r\rangle$, $\langle\beta_\theta\rangle$, $\langle\beta_\phi\rangle$, and $\langle\beta_{tot}\rangle$ (i.e. all components). Corresponding time-averaged values can be found in Table 2.

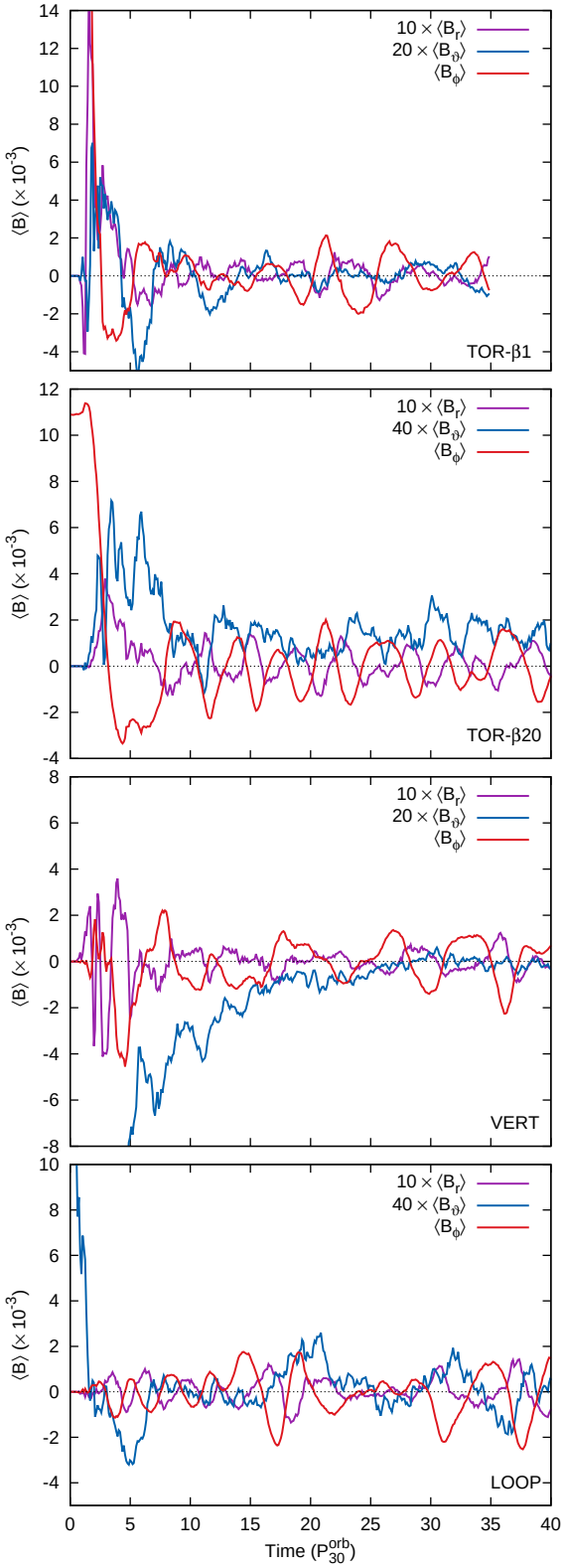

Figure 7. Mean magnetic field components for models TOR-β1 (top), TOR-β20 (upper middle), VERT (lower middle), and LOOP (bottom). Values correspond to volume-averages over the region $15 < r < 25, |z| < 2H$. To aid comparison with $\langle B_\phi \rangle$, the curves for $\langle B_r \rangle$ and $\langle B_\theta \rangle$ have been multiplied by constant factors (noted in the plots).

Focusing next on the evolution of the mean (volume-averaged) magnetic fields shown in Fig. 7, one sees both similarities and marked differences between the models. Firstly, they show different evolution for the mean vertical field, $\langle B_\theta \rangle$. The initial vertical field decays throughout the simulation for model VERT, as anticipated from the discussion of mean field evolution in § 3. Second, all models show anti-correlated, quasi-periodic oscillations in $\langle B_r \rangle$ and $\langle B_\phi \rangle$. However, these oscillations are most evident for model TOR-β20, with a weaker indication for VERT and LOOP. Thirdly, there is a suggestion of quasi-periodic oscillations in $\langle B_\theta \rangle$ for models TOR-β1, TOR-β20, and LOOP, although of quite different period, being more erratic for TOR-β20 whilst more slowly varying for LOOP. Hence, although diagnostics of the turbulence (such as $\langle \alpha_{\rm P} \rangle$ and β) do not display considerable differences between the models during their late-time evolution, the mean magnetic fields do. The intriguing implication is that the large-scale turbulent dynamo retains some memory of the initial conditions for a longer time than the turbulent stresses, and may exhibit different behaviour (on very long timescales) as a consequence. With regard to characterising the dynamo in the disk, it is noteworthy that the time-averaged radial and azimuthal fields are close to zero (Table 2), whereas the vertical field maintains a (weak) net value.

4.1.6 Do stresses correlate with vertical field?

Local (shearing-box) studies of magnetorotational turbulence indicate a correlation between the vertical field strength and the turbulent stresses (Hawley et al. 1995; Sano et al. 2004). This correlation has also been cast as a relation between the wavelength of the fastest growing vertical MRI mode and the stress (Pessah et al. 2007; Sorathia et al. 2010, 2012; Beckwith et al. 2011). Considering the ab initio vertical flux conservation inherent to the shearing-box (see § 3 and Hawley et al. 1995), it is pertinent to investigate this relation using the global models in this work.

To search for possible correlations between turbulent stresses and mean magnetic field components, in Fig. 8 we plot the data-points for $\langle \alpha_{\rm P} \rangle$ against those for $|\langle B_r \rangle|$ (left column), $|\langle B_\theta \rangle|$ (middle column), and $|\langle B_\phi \rangle|$ (right column). The points are sampled every $0.1\, P_{30}^{\rm orb}$ in time through the simulation, such that there is a relation between the clustering of points and the duration of time that a specific value was possessed by the model. The upper panel of Fig. 8 shows points for the time interval $2 < t < 10\, P_{30}^{\rm orb}$, which corresponds to the transient episode close to the start of the simulations. During this phase the models are in the process of expelling, or turbulently corrupting, the initial field configuration. As such, the vertical field initially present in models VERT and LOOP has not been entirely removed and a general trend of higher $\langle \alpha_{\rm P} \rangle$ with higher $|\langle B_\theta \rangle|$ can be seen. However, model TOR-β1 achieves the highest stresses during its transient phase ($\langle \alpha_{\rm P} \rangle \simeq 0.37$), with a less apparent correlation between $\langle \alpha_{\rm P} \rangle$ and any of $|\langle B_r \rangle|$, $|\langle B_\theta \rangle|$, or $|\langle B_\phi \rangle|$.

By the time the quasi-steady state is reached, models TOR-β1, TOR-β20, VERT, and LOOP have removed any prominent vertical field, showing similar vertical magnetic field strengths (§ 4.1.5). At these late-times ($t > 20\, P_{30}^{\rm orb}$)

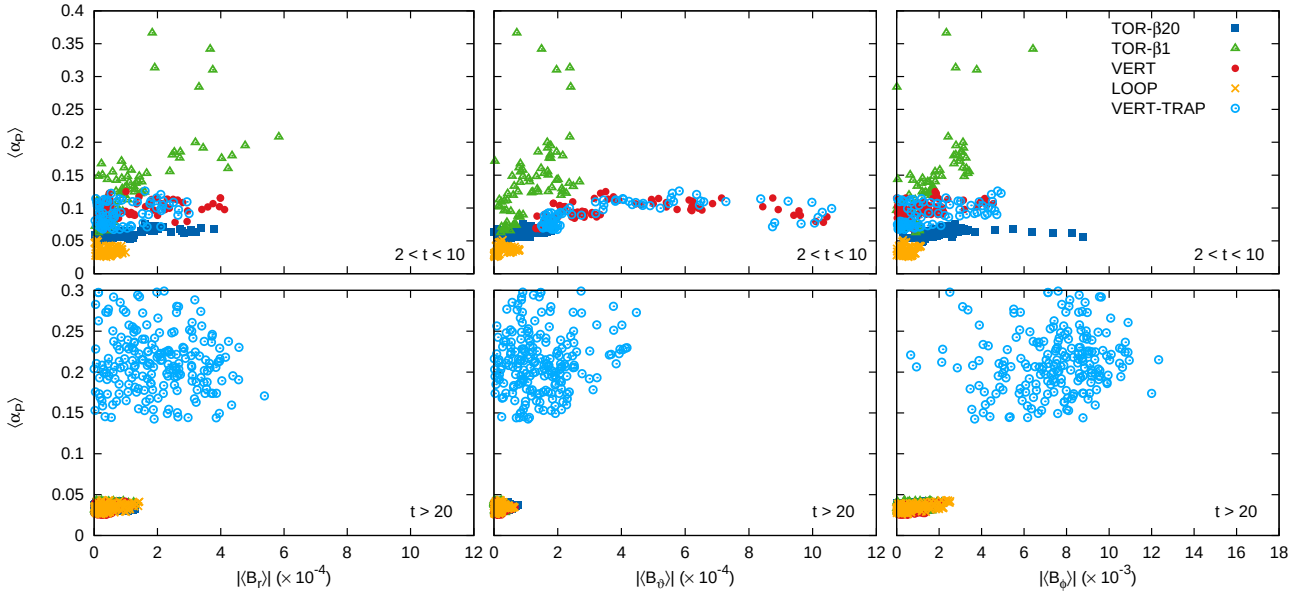

Figure 8. Correlation between the pressure-normalised stress parameter, $\langle\alpha_{\rm P}\rangle$, and the magnitude of the volume averaged magnetic field. The columns (from left to right) show the correlation with: $|\langle B_r\rangle|$, $|\langle B_\theta\rangle|$, and $|\langle B_\phi\rangle|$. The upper and lower rows show data points sampled every $0.1\,P_{30}^{\rm orb}$ from the time intervals $2 < t < 10\,P_{30}^{\rm orb}$ and $t > 20\,P_{30}^{\rm orb}$, respectively.

the data-points are heavily clustered around $\langle\alpha_{\rm P}\rangle \simeq 0.025-0.045$ and $\langle B_\theta\rangle \sim 0$.

In summary, during the transient phase close to the beginning of the runs the models suggest a correlation between $\langle\alpha_{\rm P}\rangle$ and $\langle B_\theta\rangle$. However, at later times there is little sign of such a trend, mainly due to the effective removal of a mean vertical field by the evolution of the disk. Hence, it seems less a question of whether turbulent stresses, and thus the efficiency of accretion, correlate with vertical magnetic field strength, and more one of whether a global turbulent disk retains a vertical field in the face of said accretion.

4.2 Trapping magnetic field (model VERT-TRAP)

The results of the previous section highlight the common late-time evolution for models that are initialised with different magnetic field configurations and for which the radial velocity at the inner radial edge of the disk (the simulation boundary in this case) is unconstrained. There are, however, many examples of astrophysical scenarios in which the radial velocity may be limited by large scale effects. For instance, clumping due to self-gravity in an extended disk (Shlosman & Begelman 1987; Goodman 2003; Rafikov 2009; Hopkins 2013). Also, the excessive build up of magnetic flux close to a black hole leading to a magnetically arrested disk (Narayan et al. 2003; Igumenshchev et al. 2003; Igumenshchev 2008). In this section we examine the impact of restricting the outflow of material at the inner radial disk edge using model VERT-TRAP (which adopts the viscous-outflow boundary condition described in § 2.1).

The evolution of $\langle\alpha_{\rm P}\rangle$ for model VERT-TRAP is shown in Fig. 9. Over the first $\sim 10\,P_{30}^{\rm orb}$ of the run the turbulence develops in a very similar manner to model VERT; both models display transient accretion associated with the initiation of magnetorotational turbulence in the disk, which saturates at $t \simeq 5\,P_{30}^{\rm orb}$ and gradually declines thereafter. However, in model VERT-TRAP the accretion flow builds-up at the inner radial disk edge[4], leading to a compression of magnetic field. Consequently, the magnetisation of the disk rises and with it the turbulent stress ($\langle\alpha_{\rm P}\rangle$). During the latter half of the simulation ($t > 20\,P_{30}^{\rm orb}$) $\langle\alpha_{\rm P}\rangle$ and $\beta_{\rm tot}$ reach time-averaged values of 0.21 and 1.4, respectively (Table 2). Large amplitude fluctuations for $\langle\alpha_{\rm P}\rangle$ bear similarities with those observed in strongly magnetized ($\beta \sim 1-5$) disk simulations by Machida et al. (2000). The vertical field becomes an order of magnitude more magnetized for VERT-TRAP than for VERT, with $\beta_\theta \simeq 10$ and 139 for the respective models. Strong magnetisation in the disk leads to a ratio of Maxwell-to-Reynolds stress, $-\langle B_r' B_\phi'\rangle/\langle\rho v_r' v_\phi'\rangle = 5.79$. Hence, $\langle\alpha_{\rm P}\rangle$ is considerably dominated by magnetic stresses in the field-trapped state.

The marked difference brought about by magnetic field trapping is highlighted by a comparison of the time evolution of the vertical disk structure for models VERT and VERT-TRAP in Figs. 2 and 10, respectively. Quasi-periodic oscillations are seen for model VERT-TRAP, but only at relatively early times in the run ($t \lesssim 10\ P_{30}^{\rm orb}$). For the remainder of the run the quasi-periodic oscillations cease, continuing with sporadic fluctuations. A possible explanation is that the suppression of the dynamo cycles by the onset of a strong ($\beta \lesssim 1$) magnetic field, following which a mean

[4] Suzuki & Inutsuka (2014) adopted a similar radial boundary condition at the inner grid edge but did not constrain the mass-flux to the extent that mass would build-up. Instead, they tuned their boundary condition to prevent excessive mass-loss during the initial transient whilst allowing a flow of mass consistent with the accretion rate induced by the turbulence during the quasi-steady phase.

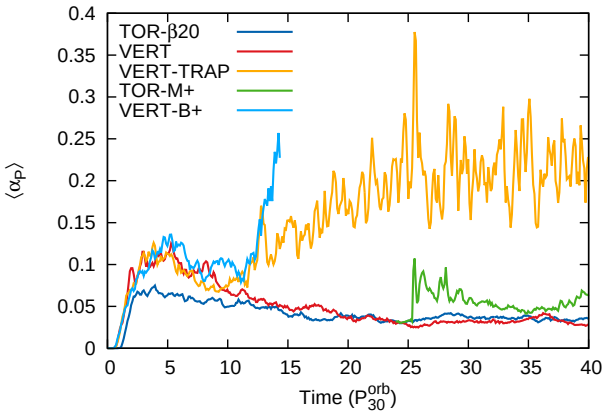

Figure 9. The time evolution of $\langle \alpha_{\rm P} \rangle$ computed for the disk body ($15 < r < 25$, $|z| < 2H$) for models TOR-β20, VERT, VERT-TRAP (§ 4.2), VERT-B+ (§ 4.3), and TOR-M+ (§ 4.4).

toroidal magnetic field develops - for further discussion of this point see Bai & Stone (2013). Strong turbulent gas velocities arise at all heights with close-to-transonic streams of gas emanating from the disk mid plane and rising into the corona.

As the turbulent activity in the disk rises, patches of the disk are seen to rotate at a sub-Keplerian rate. In Fig. 11 we show the radial profile of the fractional deviation from Keplerian rotation as a function of time, where values have been vertically and azimuthally averaged. One sees that the initial rotation profile ($t = 0$) is close to Keplerian. As turbulence establishes in the disk its rotation deviates from Keplerian, typically by 2% during the first 10 $P_{30}^{\rm orb}$. At later times, however, considerably more sub-Keplerian rotation is observed, and during the latter half of the simulation deviations of $4 - 10\%$ are seen in the radial range $10 < r < 20$. Interestingly, this coincides with the build-up of a strong magnetic field in the disk (see, e.g., Figs. 6 and 10), indicating that the additional magnetic pressure support provided by the strong field alters the disk rotation rate. Consequently, the shear rate in the disk is modified, which has implications for the growth rate of the MRI (Balbus & Hawley 1998). Also apparent from Fig. 11 is the development of sub-Keplerian rotation from smaller to larger radii, consistent with the magnetic field piling-up at the inner radial disk edge in model VERT-TRAP.

Further differences between models VERT and VERT-TRAP are apparent from an inspection of the time-averaged vertical profiles of various quantities shown in Fig. 3. The density profile for model VERT-TRAP shows a similar rounded shape close to the mid plane but the profile is much flatter between $1 < |z/H| < 2$. Both the magnetic field strength and turbulent velocities are noticeably larger for VERT-TRAP. The magnetic field is dominated by the toroidal component, and the strength of the magnetic field drops off with increasing height away from the mid plane. Similarly, the turbulent velocities fall-off with height for VERT-TRAP, however at a slower rate that in the other models.

Although the radial velocity at the inner radial disk edge is reduced in VERT-TRAP compared to VERT, the radial mass flux for VERT-TRAP is notably larger, with

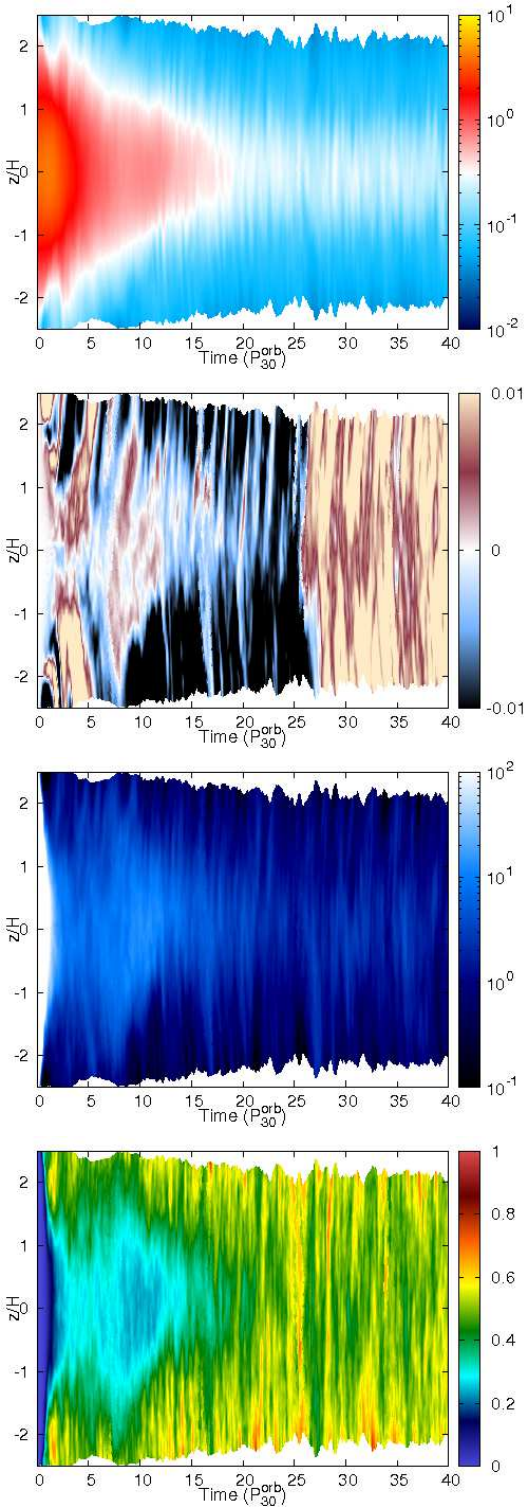

Figure 10. Same as Fig. 2 except for model VERT-TRAP

$\dot{M}_{\rm rad} = 260$ and $159\, P_{30}^{\rm orb-1}$, respectively - see Table 2. This indicates that the density of the accretion flow has increased for VERT-TRAP. At first sight this result appears at odds with the lower normalisation of the vertical density profile for VERT-TRAP compared to VERT in Fig. 3. On inspection of the simulation data, one sees that mass builds up

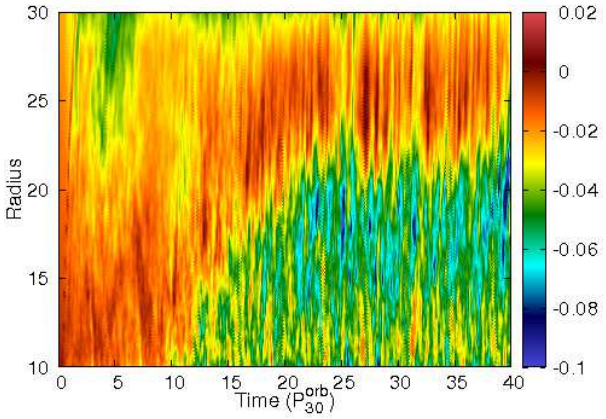

Figure 11. Time evolution of the fractional variation of the rotational velocity from Keplerian rotation, $(v_\phi - v_{\rm Kep})/|v_\phi|$ for model VERT-TRAP. The plot shows the time evolution of radial profile computed from a vertical and azimuthal averaging.

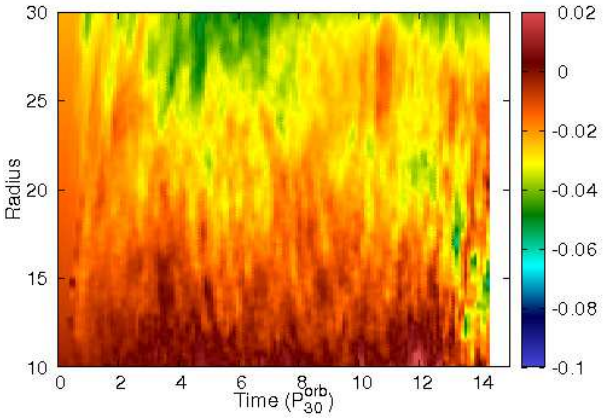

Figure 12. Same as Fig. 11 except for model VERT-B+.

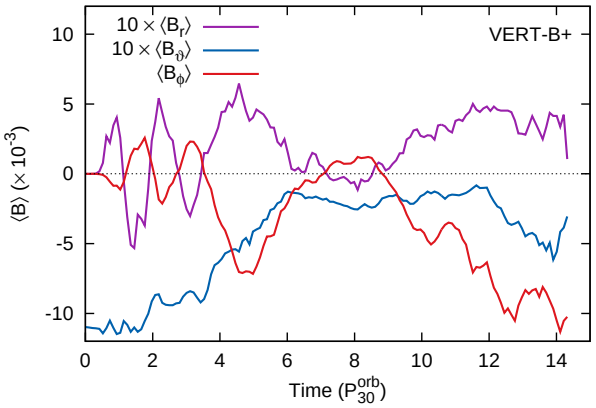

Figure 13. Same as Fig. 7 except for model VERT-B+.

at the inner radial edge of the disk, which is outside of the region averaged-over to construct the vertical profile. Interestingly, model VERT-TRAP displays a considerably larger vertical mass flux than model VERT ($\dot{M}_{\rm vert}$). In fact, vertical and radial mass fluxes differ by less than a factor of two for model VERT-TRAP. Interestingly, this suggests that the launching of a wind in a dynamically evolving turbulent disk could be instigated by a slowing of the radial accretion flow.

The evolution of mean magnetic fields proceeds differently for model VERT-TRAP compared to VERT (see Figs. 7 and 14). As previously mentioned, the mean toroidal field grows considerably up until $t \simeq 25\,P_{30}^{\rm orb}$ for VERT-TRAP, at which point a sudden sharp field reversal occurs with a corresponding spike in $\langle\alpha_{\rm P}\rangle$. Inspecting the correlation between vertical field ($|\langle B_\theta\rangle|$) and turbulent stresses ($\langle\alpha_{\rm P}\rangle$) in Fig. 8, one sees that during the initial transient phase of the simulation ($2 < t < 10\,P_{30}^{\rm orb}$) similar behaviour to model VERT is observed. However, at late times ($t > 20\,P_{30}^{\rm orb}$), a much stronger correlation between $|\langle B_\theta\rangle|$ and $\langle\alpha_{\rm P}\rangle$ is apparent.

In summary, trapping of field in a turbulent disk leads to a highly magnetized state exhibiting large, highly variable accretion stresses. In contrast, model TOR-β1 shows that an initially equipartition strength field will disperse if outflow is unconstrained. In this regard the results of model VERT-TRAP and TOR-β1 are complementary to the study of efficiently accreting ($\langle\alpha_{\rm P}\rangle \sim 0.1$), strongly magnetized ($\beta \sim 1$) disks by Johansen & Levin (2008) and Gaburov et al. (2012). Models VERT-TRAP and TOR-β1 suggest that a strongly magnetized state can only arise, and be maintained, when radial flow is constrained. This point is discussed further in § 5.2.

4.3 Injecting vertical magnetic field (model VERT-B+)

A general trend from the models in § 4.1 is that during the initial transient phase of disk evolution the field configuration is disrupted and not entirely conserved. For example, the initially purely vertical magnetic field in model VERT leaves the domain in the accretion flow and its subsequent evolution becomes similar to other models initialised with different field topologies (e.g. TOR-β20 and LOOP). In this section we use model VERT-B+ to examine the disk evolution that occurs when a weak vertical magnetic field is steadily added to the simulation domain, replenishing the field that is advected away at early times. The motivation for model VERT-B+ comes from the possibility that in astrophysical disks additional magnetic field (i.e. beyond that contained in the simulation initial conditions in this case) may flow into the disk from larger radii or, alternatively, a field component on scales much larger than the simulation domain may pervade the disk.

The setup for model VERT-B+ is identical to that of model VERT, with the exception that a constant B_θ is added to the simulation domain between $12 < r < 30$ and for all θ and ϕ. The θ-component of the magnetic field is added at a constant rate such that it would generate a $\beta = 2000$ strength field in a time interval of 40 $P_{30}^{\rm orb}$. Note that the injected B_θ is divergence-free and is added to the staggered mesh component of B_θ.

The effect of injecting a weak vertical magnetic field on the turbulent stresses is shown in Fig. 9. Up until a simulation time of $\simeq 10\,P_{30}^{\rm orb}$ the $\langle\alpha_{\rm P}\rangle$ values for models VERT-B+ and VERT are quite similar. However, from $t \sim 11\,P_{30}^{\rm orb}$ onwards the models diverge and the turbulent stress in model

VERT-B+ rises sharply. By $t = 14.4\ P_{30}^{\rm orb}$ the stress reaches $\langle \alpha_{\rm P} \rangle \simeq 0.25$ - we were unable to evolve model VERT-B+ beyond this point as the highly turbulent state of the disk proved problematic for the simulation code. As such, VERT-B+ does not reach a quasi-steady state making an analysis of time-averaged quantities/profiles difficult. From the short duration of VERT-B+ it is unclear whether additional vertical mass-loss in the form of a wind is triggered by the burst in activity at $t \gtrsim 11\ P_{30}^{\rm orb}$.

During the simulation the disk rotation deviates from Keplerian rotation (Fig. 12). Patches of sub-Keplerian rotation are observed between $20 < r < 30$ at times later than $5\ P_{30}^{\rm orb}$. However, at $t \gtrsim 10\ P_{30}^{\rm orb}$ regions of sub-Keplerian rotation also begin to extend to smaller radii, coincident with the onset of the accretion burst. Recalling the results of model VERT-TRAP where sub-Keplerian rotation was coincident with strong magnetic fields in the disk, a possible explanation for the emergence of patches of sub-Keplerian rotation in model VERT-B+ is that strong vertical field is dragged through the disk by the accretion flow. This causes a back-reaction, with further field growth leading to an increase in magnetic field, as in the classic picture of field amplification via the MRI (Balbus & Hawley 1992).

The contrast in model evolution between VERT-B+ and VERT in the time interval $11 \lesssim t \lesssim 14\ P_{30}^{\rm orb}$ does, however, highlight important differences resulting from vertical field replenishment. Firstly, it is worthwhile to note that the rate of injection of B_θ into the domain is not abrupt, yet the accumulation of additional field is sufficient to bring about a burst in accretion. During this burst phase the strength of the radial, vertical, and toroidal magnetic field components are all seen to grow, illustrated by a decrease the respective plasma-β values (Fig. 6). In essence, only a relatively weak vertical magnetic field need be injected into the disk to cause a considerable change in the accretion activity of the disk. Local shearing-box models by Bai & Stone (2013) display similar behaviour whereby the injection of a vertical magnetic field into an already turbulent disk causes considerable changes to the turbulent state. Model VERT-B+ extends this picture to global disks, albeit with a simple prescription for magnetic field injection. A detailed study of the parameter space relating to field injection (e.g., rate of field injection, topology of injection field, radius of field injection) would require additional models that are beyond the scope of the current work.

The cause of the transient outburst clearly must be related to the injection of vertical magnetic field. However, on inspection, the exact details are subtle. Firstly, if allowed to accumulate, the injected magnetic field would equate to a $\beta = 2000$ vertical field in a time span of $40\ P_{30}^{\rm orb}$. At $z = 0$ one finds from Eq (19) that $\Lambda_{\rm MRI-z}/\Delta z \approx 8.89 n_{\rm z-H} \beta_z^{-1/2}$, where Δz and $n_{\rm z-H}$ are the cell size and number of cells per scale-height in the z-direction, respectively. For $\beta_z = 2000$ one finds $\Lambda_{\rm MRI-z}/\Delta z = 8.8$, indicating adequate resolution of the fastest growing MRI mode for the initial field in models VERT, VERT-TRAP, and VERT-B+. However, the transient arises after $\simeq 11\ P_{30}^{\rm orb}$ in model VERT-B+, after which time the accumulated field would have $\Lambda_{\rm MRI-z}/\Delta z \sim 2.4$, which is borderline in terms of adequate resolution for the MRI to develop. The next clue comes from examining the mean field evolution and plasma-β for model VERT-B+. The mean vertical field in model VERT-B+ levels-off at

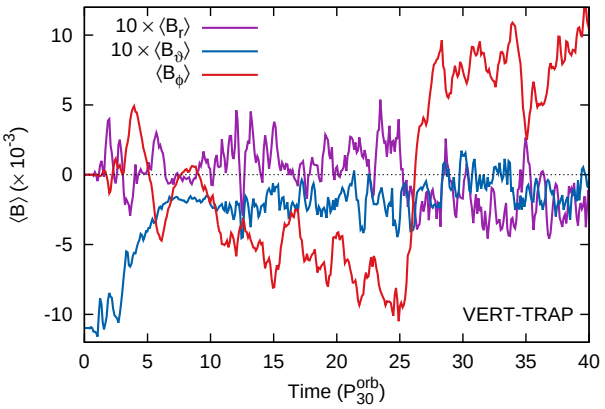

Figure 14. Same as Fig. 7 except for model VERT-TRAP.

$t \simeq 6\ P_{30}^{\rm orb}$ (see Fig. 13), in contrast to the continuing decline seen for VERT (Fig. 7). Then, at $t \simeq 11\ P_{30}^{\rm orb}$, $|\langle B_\theta \rangle|$ grows, which directly coincides with the burst in accretion activity (Fig. 9). The magnitude of the vertical field, measured by the vertical field plasma-β, also grows at this time (illustrated by a decrease in β_θ in Fig. 6). Therefore, although the accumulated field is relatively weak in terms of adequate resolution it counters the loss of field in the accretion flow to the extent that the disk evolution is altered. This may arise from the injected field building-up in dormant areas of the disk (e.g. at larger radii where the MRI takes longer to set-in initially) which, upon becoming actively turbulent, triggers a burst in accretion.

4.4 Transient accretion burst via mass injection (model TOR-M+)

The simulated disks in models TOR-β1, TOR-β20, VERT, and LOOP evolve to a similar quasi-steady turbulent state with no indication of a large amplitude recurrent burst of accretion[5]. Astrophysical disks, on the other hand, do exhibit recurring transient bursts. This variability is often attributed to thermal instability (Meyer & Meyer-Hofmeister 1981; Pringle 1981; Faulkner et al. 1983), whereby the build-up of matter during the quiescent state leads to a sudden increase in disk opacity related to the ionisation of hydrogen. Subsequently, the disk heats up and the turbulent activity rises. The compatibility of this scenario with magnetorotational turbulence has recently been demonstrated by Latter & Papaloizou (2012) and Hirose et al. (2014). From a slightly different tack, Gammie & Menou (1998) suggest that dwarf novae eruptions originate from a combination of magnetorotational turbulence with some secondary episodic (global) instability (e.g. Papaloizou & Pringle 1984).

[5] Flock et al. (2012a) argue that simulations using an azimuthal extent of $< \pi$ will be subject to recurring accretion bursts, related to an artificial build-up of low azimuthal wavenumber energy triggering a secondary phase of linear non-axisymmetric MRI growth. However, the simulations presented in this work use an azimuthal extent of $\pi/2$ with no sign of a recurrent linear-MRI phase, suggesting that run times longer than we have considered may be required for sufficient energy to build up.

Common to the above suggestions for triggering a transient burst is the build-up of mass in the disk. In this section we examine the results of a supplementary simulation (model TOR-M+) which tests the response of a turbulent magnetic global disk to the rapid addition of zero angular momentum mass. This model uses the state of TOR-β20 at $t = 25\,P_{30}^{\rm orb}$ for its initial conditions. Then, in the interval $25 < t < 26\,P_{30}^{\rm orb}$ the mass source term (described in § 2.1) is modified to: i) relax the density towards twice that of the initial conditions, and, ii) conserve angular momentum in density increments, $\delta\rho$, such that the azimuthal velocity, v_ϕ, is respectively modified by $\delta v_\phi = -v_\phi \delta\rho/(\rho + \delta\rho)$. We note that model TOR-M+ is also applicable for understanding the subsequent disk evolution following stochastic accretion in the disk tearing scenario proposed by Nixon et al. (2012, 2013).

Shortly after the enhanced mass injection commences the disk undergoes a transient burst of accretion activity and a sharp rise in $\langle\alpha_{\rm P}\rangle$ for model TOR-M+ at $t \simeq 25\,P_{30}^{\rm orb}$ (Fig. 9). $\langle\alpha_{\rm P}\rangle$ subsequently decays, with a mild recurrence at $t \simeq 40\,P_{30}^{\rm orb}$, possibly related to clumps of mass compressing magnetic field as they advect through the disk. This premise is supported by $\beta_{\rm tot}$ falling to $\simeq 7$ at this time (compared to $\beta_{\rm tot} \simeq 18$ for model TOR-β20) - see Fig. 6 and Table 2. Examining the vertical structure of the disk in model TOR-M+ (see Fig. 3) it bears close similarity to model TOR. The most notable difference is in the strength of the magnetic field, which is clearly stronger in all components for model TOR-M+ compared to TOR, but more apparently so for the radial and vertical field.

The mechanism that triggers the outburst is two-fold. Firstly, increasing the density reduces the Alfvén speed, which in turn reduces the wavelength of the fastest growing MRI mode (see Eq 19). This opens up additional fast growing, short wavelength MRI modes which can inject energy on the smallest scales. Secondly, reducing the azimuthal velocity in regions where mass is added causes gravitational attraction to exceed the centrifugal force. Hence, over-dense regions move radially inwards, dragging field lines with them which are then sheared. The result is a rise in radial field followed by conversion to toroidal field, both of which act to enhance the turbulent stresses.

5 DISCUSSION

5.1 How big is α?

The stresses produced by magnetorotational turbulence effectively transport angular momentum. However questions have been raised about whether the level of angular momentum transport produced by MRI-driven turbulence (quantified by $\langle\alpha_{\rm P}\rangle$) is actually sufficient to explain observations of astrophysical accretion disks. For example, King et al. (2007) compiled results from shearing-box studies and highlighted a disparency between simulated $\langle\alpha_{\rm P}\rangle$ values of $\lesssim 0.01$ and observationally inferred values of $\langle\alpha_{\rm P}\rangle \simeq 0.1 - 0.3$ for post-outburst dwarf novae disks.

There are some important points to note about this discrepancy. Firstly, unstratified shearing-box studies with a net vertical field display $\langle\alpha_{\rm P}\rangle$ values as high as 0.2-0.7 (Hawley et al. 1995; Sano et al. 2004; Simon et al. 2009). However, a typical consequence of a net vertical field is a disk wind, whereas a number of the objects discussed by King et al. (2007) show no evidence of a wind, jet, or large-scale vertical field of any description.

The evolution of a global disk threaded with a net vertical field has been explored in this work - see also Beckwith et al. (2009) and Suzuki & Inutsuka (2014). Interestingly, during the transient phase of model TOR-β1, $\langle\alpha_{\rm P}\rangle$ reaches values as high as ~ 0.37, with no associated disk wind (i.e. the vertical-to-radial mass flux ratio is small). At late-times in the simulation the net vertical field has been effectively removed, slipping away in the accretion flow, and irrespective of the initial field configuration one finds $\langle\alpha_{\rm P}\rangle \simeq 0.032 - 0.036$. A similar range of values for $\langle\alpha_{\rm P}\rangle$ is seen in previous global disk simulations. For example, Suzuki & Inutsuka (2014) find $\langle\alpha_{\rm P}\rangle \sim 0.01 - 0.02$ during the late-time evolution, whereas the study by Hawley et al. (2013) (for which the models are not evolved beyond the initial transient phase) reports $\langle\alpha_{\rm P}\rangle$ as high as 0.15. Taking stock of the above results, there is an obvious suggestion that magnetorotational turbulence can produce sufficiently large $\langle\alpha_{\rm P}\rangle$ values to gain agreement with observation. However, the disk must either be made to undergo a transient burst, or, a net vertical field must be retained/replenished over dynamically significant timescales. We have demonstrated the viability of these channels with models TOR-M+, VERT-TRAP, and VERT-B+, which produce $\langle\alpha_{\rm P}\rangle \simeq 0.1 - 0.25$.

5.2 External/environmental influence

An isolated disk will evolve to a common quasi-steady turbulent state, irrespective of the initial conditions and/or initial disturbance to the disk. This is illustrated by models TOR-β20, TOR-β1, VERT, and LOOP, for which statistical measures of the turbulence are similar during the late-time disk evolution (see also Parkin & Bicknell 2013a, where the influence of different initial perturbations is examined). As discussed in the previous section, astrophysical disks do exhibit transient evolution and in some cases changes in the accretion state. Model VERT-TRAP shows that altering the rate that mass and magnetic field can leave the disk can cause abrupt changes to the accretion state. In essence, events occurring exterior to the disk can directly influence the accretion state by regulating the inflow/outflow of material/field.

All of this points to the importance of the environment outside of the disk. One must then give consideration to the timescale(s) associated with the external process(es). For example, if the disk expels magnetic flux in the accretion flow at a rate faster than it can be digested by the central object, be it a star or a black hole, then the build-up of magnetic flux may impinge on the disk (e.g. Igumenshchev et al. 2003; Romanova et al. 2012). Furthermore, accretion of magnetized gas onto the disk at a rate faster than it can be processed by the turbulence can lead to a strongly magnetized state (Gaburov et al. 2012).

The environment surrounding the accretion disk may enforce preservation of field topology, or provide a source of poloidal magnetic flux into the disk over a dynamically important timescale. For example, the conservation of magnetic flux in collapse scenarios (Bisnovatyi-Kogan & Ruzmaikin 1974, 1976; Mouschovias 1976), accretion of magnetic field in a galactic nucleus (Proga & Begelman 2003),

or wind accretion in a binary system (Frank et al. 2002). Global models similar to those presented in this study could be readily augmented to examine these scenarios.

5.3 Wind launching

Launching a wind from a turbulent magnetized disk remains a challenging problem. Recent studies adopting shearing-box models have demonstrated that vertical outflows arise from a patch of a turbulent disk if initialised with a net flux vertical field (Suzuki & Inutsuka 2009; Ogilvie 2012; Moll 2012; Lesur et al. 2013; Fromang et al. 2013; Bai & Stone 2013). However, the radially periodic shearing-box boundary conditions preserve the net vertical field topology (see § 3). In contrast, the vertical field in model VERT exits the disk in the accretion flow (see also Suzuki & Inutsuka 2014) and during the quasi-steady state the ratio of vertical-to-radial mass flux is $\sim 11\%$. Model VERT-TRAP, on the other hand, shows that if the radial flow out of the disk is constrained (so as to trap vertical and azimuthal field) then the vertical-to-radial mass flux reaches $\sim 59\%$. Hence, the results indicate that time-steady disks do not launch winds if the radial flow is unconstrained, whereas wind-launching may be triggered if the rate at which vertical/azimuthal field exits the disk is impeded (compared to the steady-state rate).

6 CONCLUSIONS

The dependence of turbulent stresses on initial field configuration, magnetic field trapping due to inhibited radial outflow, magnetic field injection, and rapid mass injection has been investigated using global MHD disk simulations. Properties of the saturation stress level during the early-time transient phase of disk evolution show a dependence on the initial magnetic field. This finding is consistent with models presented by Hawley et al. (2013) which focused on the transient phase during roughly the first $\simeq 10.3\,P_{30}^{\rm orb}$ of the simulation. However, a major new result in this work, and one which was achieved by utilising a mass source term to avoid the exhaustion of disk mass by ongoing accretion, is that irrespective of the strength and topology of the initial magnetic field an *isolated* magnetorotationally turbulent disk evolves to a statistically similar quasi-steady state that is characterised by: i) a volume-averaged stress-to-gas-pressure ratio, $\langle\alpha_{\rm P}\rangle \simeq 0.032 - 0.036$, ii) a gas-to-magnetic pressure ratio, $\beta \simeq 16 - 18$, and, iii) zero-net time-averaged radial and azimuthal magnetic fields.

Simulations exploring the influence of trapping of magnetic field, vertical field injection, and of rapid mass injection, on the turbulence reveal that these mechanisms lead to relatively large stresses in the disk. Trapping of magnetic field produces a strongly magnetized disk with $\langle\alpha_{\rm P}\rangle \sim 0.2$ and considerable vertical mass flux in the form of an intermittent wind. The injection of a vertical magnetic field, even a relatively weak one that equates to an accumulation of a $\beta = 2000$ field over a time interval of 40 $P_{30}^{\rm orb}$, is sufficient to trigger a burst in accretion with stresses reaching $\langle\alpha_{\rm P}\rangle \sim 0.25$. Rapid mass injection leads to a sudden sharp increase in turbulent stresses, peaking at $\langle\alpha_{\rm P}\rangle \sim 0.1$ and subsequently decaying to the pre-outburst level. The results of these simulations may be relevant for understanding accretion state changes, transient bursts, and large observationally inferred accretion efficiencies for astrophysical disks. Indeed limit cycle behaviour reminiscent of dwarf novae eruptions could be produced with the inclusion of a temperature (and perhaps also surface density) dependent resistivity, following similar suggestions by Balbus & Lesaffre (2008), Lesaffre et al. (2009), and Latter & Papaloizou (2012).

Acknowledgements

I thank Geoffrey Bicknell, Yuri Levin, and Daniel Price for helpful discussions, the Australian Research Council's Discovery Projects scheme (project number DP1096417) for financial support, and the National Computational Infrastructure for computational resources through access to the Raijin supercomputer.

REFERENCES

Bai, X.-N. & Stone, J. M. 2013, ApJ, 767, 30
Balbus, S. A. & Hawley, J. F. 1991, ApJ, 376, 214
Balbus, S. A. & Hawley, J. F. 1992, ApJ, 400, 610
Balbus, S. A. & Hawley, J. F. 1998, Reviews of Modern Physics, 70, 1
Balbus, S. A. & Lesaffre, P. 2008, NewAR, 51, 814
Beckwith, K., Armitage, P. J., & Simon, J. B. 2011, MNRAS, 416, 361
Beckwith, K., Hawley, J. F., & Krolik, J. H. 2008, ApJ, 678, 1180
Beckwith, K., Hawley, J. F., & Krolik, J. H. 2009, ApJ, 707, 428
Bisnovatyi-Kogan, G. S. & Ruzmaikin, A. A. 1974, Ap&SS, 28, 45
Bisnovatyi-Kogan, G. S. & Ruzmaikin, A. A. 1976, Ap&SS, 42, 401
Brandenburg, A., Nordlund, A., Stein, R. F., & Torkelsson, U. 1995, ApJ, 446, 741
Colella, P. & Woodward, P. R. 1984, J. Comput. Phys, 54, 174
Davis, S. W., Stone, J. M., & Pessah, M. E. 2010, ApJ, 713, 52
Faulkner, J., Lin, D. N. C., & Papaloizou, J. 1983, MNRAS, 205, 359
Flock, M., Dzyurkevich, N., Klahr, H., Turner, N., & Henning, T. 2012a, ApJ, 744, 144
Flock, M., Dzyurkevich, N., Klahr, H., Turner, N. J., & Henning, T. 2011, ApJ, 735, 122
Flock, M., Henning, T., & Klahr, H. 2012b, ApJ, 761, 95
Frank, J., King, A., & Raine, D. J. 2002, Accretion Power in Astrophysics: Third Edition
Fromang, S., Latter, H., Lesur, G., & Ogilvie, G. I. 2013, A&A, 552, A71
Fromang, S. & Nelson, R. P. 2006, A&A, 457, 343
Fromang, S. & Papaloizou, J. 2007, A&A, 476, 1113
Gaburov, E., Johansen, A., & Levin, Y. 2012, ApJ, 758, 103
Gammie, C. F. & Menou, K. 1998, ApJL, 492, L75
Gardiner, T. A. & Stone, J. M. 2005, Journal of Computational Physics, 205, 509

Goodman, J. 2003, MNRAS, 339, 937
Goodman, J. & Xu, G. 1994, ApJ, 432, 213
Gressel, O. 2010, MNRAS, 405, 41
Gressel, O., Nelson, R. P., Turner, N. J., & Ziegler, U. 2013, ApJ, 779, 59
Guan, X., Gammie, C. F., Simon, J. B., & Johnson, B. M. 2009, ApJ, 694, 1010
Guilet, J. & Ogilvie, G. I. 2012, MNRAS, 424, 2097
Hawley, J. F. 2000, ApJ, 528, 462
Hawley, J. F., Gammie, C. F., & Balbus, S. A. 1995, ApJ, 440, 742
Hawley, J. F., Guan, X., & Krolik, J. H. 2011, ApJ, 738, 84
Hirose, S., Blaes, O., Krolik, J. H., Coleman, M. S. B., & Sano, T. 2014, arxiv:1403.3096
Hawley, J. F., Richers, S. A., Guan, X., & Krolik, J. H. 2013, ApJ, 772, 102
Hopkins, P. F. 2013, MNRAS, 430, 1653
Igumenshchev, I. V. 2008, ApJ, 677, 317
Igumenshchev, I. V., Narayan, R., & Abramowicz, M. A. 2003, ApJ, 592, 1042
Johansen, A. & Levin, Y. 2008, A&A, 490, 501
King, A. R., Pringle, J. E., & Livio, M. 2007, MNRAS, 376, 1740
Kuncic, Z. & Bicknell, G. V. 2004, ApJ, 616, 669
Latter, H. N. & Papaloizou, J. C. B. 2012, MNRAS, 426, 1107
Lesaffre, P., Balbus, S. A., & Latter, H. 2009, MNRAS, 396, 779
Lesur, G., Ferreira, J., & Ogilvie, G. I. 2013, A&A, 550, A61
Lubow, S. H., Papaloizou, J. C. B., & Pringle, J. .E 1994, MNRAS, 267, 235
Lynden-Bell, D. & Pringle, J. E. 1974, MNRAS, 168, 603
Machida, M., Hayashi, M. R., & Matsumoto, R. 2000, ApJL, 532, L67
McKinney, J. C., Tchekhovskoy, A., & Blandford, R. D. 2012, MNRAS, 423, 3083
Meyer, F. & Meyer-Hofmeister, E. 1981, A&A, 104, L10
Mignone, A., Bodo, G., Massaglia, S., Matsakos, T., Tesileanu, O., Zanni, C., & Ferrari, A. 2007, ApJS, 170, 228
Mignone, A., Flock, M., Stute, M., Kolb, S. M., & Muscianisi, G. 2012, A&A, 545, A152
Miyoshi, T. & Kusano, K. 2005, J. Comput. Phys, 208, 315
Moll, R. 2012, A&A, 548, A76
Mouschovias, T. C. 1976, ApJ, 206, 753
Narayan, R., Igumenshchev, I. V., & Abramowicz, M. A. 2003, PASJ, 55, L69
Nixon, C., King, A., & Price, D. 2013, MNRAS, 434, 1946
Nixon, C., King, A., Price, D., & Frank, J. 2012, ApJL, 757, L24
Noble, S. C., Krolik, J. H., & Hawley, J. F. 2010, ApJ, 711, 959
Ogilvie, G. I. 2012, MNRAS, 423, 1318
Papaloizou, J. C. B. & Pringle, J. E. 1984, MNRAS, 208, 721
Parkin, E. R. 2014, MNRAS, 438, 2513
Parkin, E. R. & Bicknell, G. V. 2013a, ApJ, 763, 99
Parkin, E. R. & Bicknell, G. V. 2013b, MNRAS, 435, 2281
Pessah, M. E., Chan, C.-k., & Psaltis, D. 2007, ApJL, 668, L51
Pringle, J. E. 1981, ARA&A, 19, 137
Proga, D. & Begelman, M. C. 2003, ApJ, 592, 767
Rafikov, R. R. 2009, ApJ, 704, 281
Rider, W. J., Greenough, J. A., & Kamm, J. R. 2007, J. Comput. Phys, 225, 1827
Romanova, M. M., Ustyugova, G. V., Koldoba, A. V., & Lovelace, R. V. E. 2012, MNRAS, 421, 63
Sano, T., Inutsuka, S.-i., Turner, N. J., & Stone, J. M. 2004, ApJ, 605, 321
Shakura, N. I. & Sunyaev, R. A. 1973, A&A, 24, 337
Shi, J., Krolik, J. H., & Hirose, S. 2010, ApJ, 708, 1716
Shlosman, I. & Begelman, M. C. 1987, Nature, 329, 810
Simon, J. B., Beckwith, K., & Armitage, P. J. 2012, MNRAS, 422, 2685
Simon, J. B., Hawley, J. F., & Beckwith, K. 2009, ApJ, 690, 974
Sorathia, K. A., Reynolds, C. S., & Armitage, P. J. 2010, ApJ, 712, 1241
Sorathia, K. A., Reynolds, C. S., Stone, J. M., & Beckwith, K. 2012, ApJ, 749, 189
Stone, J. M., Hawley, J. F., Gammie, C. F., & Balbus, S. A. 1996, ApJ, 463, 656
Suzuki, T. K. & Inutsuka, S.-i. 2009, ApJL, 691, L49
Suzuki, T. K. & Inutsuka, S.-i. 2014, ApJ, 784, 121
Tchekhovskoy, A., Narayan, R., & McKinney, J. C. 2011, MNRAS, 418, L79